A Coherent Point Drift Algorithm for Breast Image Registration via Surface Markers

by

Ghazaleh Ahmadian

A Thesis Submitted in Partial Fulfillment
of the Requirements for the Degree of Master of Science in
Modelling and Computational Science
University of Ontario Institute of Technology
March 2017

Supervisors

Professor Mehran Ebrahimi

Professor C. Sean Bohun

Abstract

Breast Magnetic Resonance Imaging (MRI) is a reliable imaging tool for localization and evaluation of lesions prior to breast conserving surgery (BCS). MR images typically will be used to determine the size and location of the tumours before making the incision in order to minimize the amount of tissue excised. The arm position and configuration of the breast during and prior to surgery are different and one question is whether it would be possible to match the two configurations. This matching process can potentially be used in development of tools to guide surgeons in the incision process. Recently, a Thin-Plate-Spline (TPS) algorithm has been proposed to assess the feasibility of breast tissue matching using fiducial surface markers in two different arm positions. The registration algorithm uses the surface markers only and does not employ the image intensities. In this Thesis, I apply and evaluate a coherent point drift (CPD) algorithm for registration of 3D breast MR images of six patient volunteers. In particular, we evaluate the results of the previous TPS registration technique to the proposed rigid, affine, and deformable CPD registration algorithms on the same patient datasets. The results suggest that the CPD deformable registration algorithm is superior in correcting the motion of the breast compared to CPD rigid, affine and TPS registration algorithms. The CPD registration results reported in this thesis took 0.2 to 0.4 seconds, which is significantly lower than the computation time using TPS (under a minute).

Acknowledgments

First, I would like to express my sincere gratitude to my supervisors Drs. Mehran Ebrahimi and C. Sean Bohun for all their support, help, and directions. Their advice and inspirations were the light during this project and will be with me for my entire life.

I would like to thank Dr. Anne Martel (Sunnybrook Research Institute, Toronto, Ontario, Canada) for providing the volunteer patient datasets. I would like to thank Dr. Jan Moderstizki for sharing his image registration codes with us.

I would also like to express my gratitude to my friends and classmates whose support, insights and company will always be remembered.

Finally, heartfelt thanks go to my parents who have always encouraged and supported me with their infinite love.

Contents

List of Tables

List of Figures

List of Acronyms

MRI Magnetic Resonance Imaging

BCS Breast Conserving Surgery

CPD Coherent Point Drift

TPS Thin Plate Spline

ICP Iterative Closest Point

OR Operation Room

CT Computed Tomography

SPECT Single Photon Emission Computed Tomography

PET Positron Emission Tomography

X-ray X-radiation

Chapter 1

Introduction

1.1 Image Registration

Image registration is the task of aligning one image to another image. In a day and age where cameras are ubiquitous items, registration techniques find applications in many areas, such as image stitching applications [SF00,Bro92,ZF03]. Another important application of image registration is in a clinical setting, where imaging equipment are indispensable diagnostic tools. It is useful at times for physicians to obtain images of the same region with different imaging methods, such as X-rays and magnetic resonance imaging (MRI), since different imaging methods contrast various body tissues differently. To extract information from two images taken at different times, it may be necessary to align or register

the images together to see certain features in relation to other anatomical features. The procedure involves a geometric transformation that includes matching of corresponding points or image features on the images by trying to maximize the similarity between such points or the images while estimating the transformation parameters. A typical image registration algorithm consists of four components: (1) a similarity measure that penalizes the dissimilarity between the two images; (2) a series of geometric transformations that can be applied to the moving image for the spatially warping step; (3) an optimizer that searches for the optimized transformation that maximizes the similarity; and (4) an interpolator that interpolates image intensities at non-grid locations of the transformed moving image [Bro92, SLZ+12, MV98].

1.2 Types of Images

The term "Medical Image" covers a wide variety of types of images, with very different underlying physical principles, and very different applications. The sort of images used in health care and medical research vary from microscopic images of histological sections to video images used for remote consultation, and from images of the eye taken with a camera to whole body radioisotope images. In principle, medical image registration could involve bringing all the information from a given patient, whatever the form, together into a sin-

gle representation record. Recent developments in medical image registration have been driven less by this dream of unifying image information than by the practical desire to make better use of certain types of image information for specific clinical applications or in medical research. The main radiological imaging modalities includes traditional projection radiographs, with or without contrast and subtraction, nuclear medicine projection images, ultrasound images and the cross-sectional modalities of x-ray computed tomography (CT), magnetic resonance imaging (MRI), single photon emission computed tomography (SPECT) and positron emission tomography (PET).

We refer to the MRI modality in this thesis which is a medical imaging technology that uses radio waves and a magnetic field to create detailed images of organs and tissues. Furthermore, MRI has proven to be highly effective in diagnosing a number of conditions by showing the difference between normal and diseased soft tissues of the body. MRI is often used to visualize blood vessels, abnormal tissue, breasts, bones and joints, organs in the pelvis, chest and abdomen (heart, liver, kidney, spleen), spinal injuries, tendon and ligament tears [BKZ04].

1.3 Image Registration Methods

Image registration is the process of finding a transformation on the coordinates of the pixels or voxels of one image to align it to another. Registration techniques can generally be divided into two categories:

1. Landmark-based registration

   Landmark-based or geometry-based methods use markers or features of the image and track the movement of these markers or features. Because landmark-based methods rely on features in the image, such methods require fiducial markers[1] or segmentation to be performed beforehand. On the other hand, a set of corresponding fiducial pairs are selected to specify a transformation that aligns the points. The fiducials are localized by interactive visual identification of anatomical landmarks. Commonly used methods for aligning two sets of corresponding fiducial points involve iterative closest point (ICP) [BM92] and thin plate spline (TPS) [B$^+$89]. ICP was proposed to represent a key approach for registering $3D$ shapes (including free-form curves and surfaces), which minimizes the distance from the source to the reference points. TPS defines a unique smooth registration from a template image to a target image based on registering corresponding landmarks.

[1] Fiducial marker placement uses imaging guidance to place small metal objects called fiducial markers in or near a tumor in preparation for performing MR imaging.

The methods of aligning two sets of corresponding points on the surfaces are similar to the point- based registration methods. It involves determining corresponding surfaces in different images (and/or physical space) and computing the transformation that best aligns these surfaces [SF00]. The surface representation can be simply a point set (i.e. a collection of points on the surfaces), a faceted surface (e.g. triangle set), an implicit surface, or a parametric surface.

2. Intensity-Based Methods

   Intensity-based methods perform registration based on pixel or voxel intensities of the images and do not single out features. Hence, the transformation of intensity-based registration is determined by iteratively optimizing the similarity measure, which is calculated from all pixel or voxel intensity values [SF00].

This thesis will solely relate to landmark-based methods.

1.4 Objective

Breast Magnetic Resonance Imaging (MRI) is a reliable imaging tool for localization and evaluation of lesions prior to breast conserving surgery (BCS).

Usually, breast MRI is performed in the prone position, where the breasts are pendant into the imaging coils to overcome motion artifacts from respiration thereby providing high

resolution imaging. However in this configuration, the breast shape is different compared to the actual configuration in the operating room table [ESM+14]. A goal is to develop a computer assisted surgery (CAS) tool by assigning correspondences between two configurations to recover the transformation that maps one to the other. The results in [ESM+14] are based on matching of two configurations, namely *supine arm up* and *supine arm down* positions. Specifically, the scheme applies fiducial surface markers in these two different arm positions that describe the breast surface. The registration algorithm uses the surface markers only and does not employ the image intensities. The aim of the algorithm is to find the correspondence between the markers as well as the transformation that matches one configuration to the other. Although, we only try to find the map between markers which are placed on the surface of breasts, internal breast tissues including the tumour inside are connected to the surface. One Movement even internal or external affects another.

In addition, the comparison between pre-operative images and intra-operative images is essential to image-guided procedures. Intra-operative images provide live positional updates, while pre-operative images provide important anatomical details.

In this thesis, we apply a probabilistic method, called the Coherent Point Drift (CPD), introduced by Myronenko et al. [MS10], for rigid, affine and deformable point set registration on the three-dimensional ($3D$) breast MRI datasets of six patient volunteers in [ESM+14]. We then determine the accuracy and computational time of the three

CPD registration algorithms and provide a comparison between these and the TPS algorithm [ESM+14].

1.5 Literature Survey

1.5.1 Introduction to the Registration in Medical Applications

While the incidence and mortality rates of breast cancer vary internationally, currently it is the most commonly diagnosed cancer among women in most parts of the world [JCDW10]. In Canada, breast cancer accounts for the second cause of cancer deaths despite the significant improvement in survival rates since the mid-80s [SoCACoRR87]. Currently the 5-year survival rate is 87%, likely as a result of advances in treatment and breast cancer screening. Breast cancer develops through multiple stages and the reason why some tumors eventually become invasive and metastatic and some of them remain non-invasive pre-cancers is still under investigation. Thus, detection, diagnosis and interventions could benefit from combining information from different images or aligning images. To achieve this goal, establishing accurate correspondence between images or between images and a real world setting is required. The breast is a soft organ and is subject to large deformations when the patient position is changed. Different procedures require different patient setups to optimize image acquisition (e.g prone Magnetic Resonance Imaging),

improve patient stability and comfort (e.g supine radiotherapy treatment) or account for practical circumstances (e.g. supine surgical position).

Many papers have been published presenting methods to extract or present a surface before applying surface-based registration methods. In general, the surface can be represented by parameterizing the surface. Then the difference between B-spline and polynomial become obvious [CC78]. The control in shape change is better achieved with B-spline curves than the polynomial curves. The degree of the curve is not dependent on the total number of points. B-splines are made of several curve segments that are joined "smoothly." Each such curve segment is controlled by a couple of consecutive control points. Thus, a change in the position of a control point only propagates upto a predictable range. Based on the brief given explanation, B-spline, which is the method related to the parametric surface, is a global method and the polynomial is a local one. We are looking to apply a piecewise method in order to have a large deformation available in this research.

Thus, the surface can be represented as a cloud of points or a triangulated surface. In this situation interpolation is required, incrementing the computing time and decrementing the quality of the point signature. Surface meshing techniques are general way to create a surface out of points, and currently there are two algorithms provided: a very fast triangulation of the original points, and a slower meshing that does smoothing and hole filling as well. Creating a convex hull [BDH96, PH77] is useful for example when there is a

need for a simplified surface representation or when boundaries need to be extracted.

Also, many algorithms exist for rigid and non-rigid alignment of point sets or images [Mod09] and many papers have been published presenting these algorithms to register two configurations to find a reasonable transformation that maps one configuration to another. A general reviews and surveys of these can be found in [Sti86,Pea94,PBSS00,LH03,Tan05].

1.5.2 Iterative Closest Point Algorithm

The Iterative Closest Point (ICP) algorithm was introduced in 1991 by Chen and Medioni [CM92] and independently by Besl and McKay [BM92] and it was further developed by various researchers. ICP algorithm is one of the most popular methods for rigid point set registration due to its simplicity and low computational complexity. ICP iteratively assigns correspondences based on a closest distance criterion and finds the least-squares rigid transformation relating the two point sets. In this work, the model point set will be denoted $Q = \{q_1, q_2, ..., q_N\}$ and the data point set $P = \{p_1, p_2, ..., p_N\}$. In each iteration step, the algorithm selects the closest points as correspondences and calculates the transformation, normally rotation (R) and translation (T). In order to formulate the goodness of fit mathematically, an error metric, or objective function E is defined.

$$E = \sum_{i=1}^{N} w_{i,j} \|Rp_i + T - q_i\|^2. \tag{1.1}$$

R and T represent rotation and translation. $w_{i,j}$ are the weights. These are presented as $w_{i,j} = 1$, if q_i is the closest point to p_i and $w_{i,j} = 0$ otherwise.

1.5.3 Thin Plate Spline Algorithm

In this section, a detailed description of the TPS landmark-based registration is presented. The idea of TPSs was initially introduced in the pioneering work of Duchon [Duc76] and was later employed for image registration such as Fair book [Mod09] and the articles within. Let $t_j = [t_j^1, t_j^2, t_j^3]$ denote the position of the j^{th} landmark located during surgery (in this study this is taken to be the location of the markers in the arm up image) and $r_j = [r_j^1, r_j^2, r_j^3]$ the position of the corresponding landmark in the pre-surgical image, $j = 1, 2, \ldots, n$, where n is the number of given landmarks. The goal is to find the transformation $y : \mathbb{R}^3 \to \mathbb{R}^3$, such that

$$y(r_j) = t_j \qquad \text{for all} \qquad j = 1, 2, \ldots, n \tag{1.2}$$

which minimizes the objective function

$$S[y] = \int_\Omega \sum_{i,p,q=1}^{3} \left(\partial_{p,q} y^i(x)\right)^2 \mathrm{d}x. \tag{1.3}$$

This is the linearized bending energy of a thin plate in $3D$, where p and q are coordinates, that imposes some kind of smoothness on y. It has been shown [Duc76] that the solution of component y^i of the unknown transformation y belongs to a certain space that is spanned by shifts of an a-priori known function and a polynomial correction term. To be precise, in $3D$

$$y^i(x) = \sum_{j=1}^{n} c_j^i \|x - r_j\| + \omega_0^i + \omega_1^i x^1 + \omega_2^i x^2 + \omega_3^i x^3, \qquad i = 1, 2, 3. \tag{1.4}$$

Fortunately the solution can be obtained by solving a linear system of equations to evaluate the coefficients of this expression. If we define $A = [\|r_k - r_j\|] \in \mathbb{R}^{n,n}$, $t^i = [t_1^i, t_2^i, t_3^i]^\mathsf{T} \in \mathbb{R}^{n,1}$, $c^i = [c_1^i, c_2^i, \ldots, c_n^i]^\mathsf{T} \in \mathbb{R}^{n,1}$, $\omega^i = [\omega_0^i, \omega_1^i, \omega_2^i, \omega_3^i]^\mathsf{T} \in \mathbb{R}^{4,1}$ and $B = [e, r] \in \mathbb{R}^{n,4}$, where $e = [1, ..., 1]^\mathsf{T} \in \mathbb{R}^{n,1}$, $r = [r_j^i] \in \mathbb{R}^{n,3}$, the landmark correspondence and the transformation energy minimization condition yields

$$\begin{bmatrix} A & B \\ B^\mathsf{T} & 0_{4,4} \end{bmatrix} \begin{bmatrix} c^i \\ \omega^i \end{bmatrix} = \begin{bmatrix} t^i \\ 0_{4,1} \end{bmatrix} \tag{1.5}$$

for $i = 1, 2, 3$, see [Mod09].

Hence, by substituting the evaluated coefficients c^i, w^i we can determine y^i as well as the desired unknown transformation y.

Chapter 2

Datasets Visualization

2.1 Breast Anatomy

The breast is a modified skin gland that lies on top of the musculature that encases the chest wall. The breast is not completely separated from these muscles, in fact only a layer of adipose tissue and connective fascia separate the breast from the pectoral muscle.

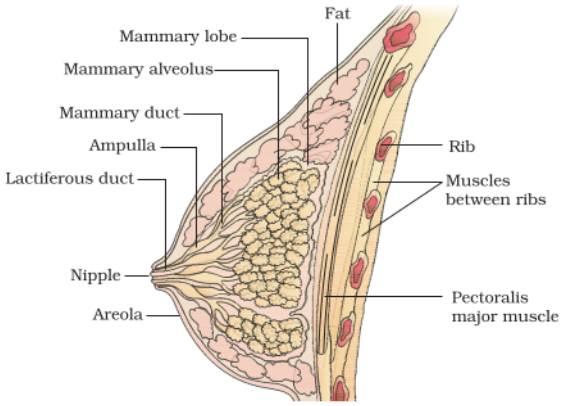

Figure 2.1: Anatomy of the breast which is taken from [LLC09a].

The breast is composed of three major tissue types: glandular tissue (parenchyma), fibrous stroma and fatty tissue. The stroma is composed of connective tissue, ligaments, blood vessels, lymphatics, lymph nodes, and nerves [ML05] and its main function is to provide support and to nurture the breast. The glandular tissue is organized in a ductal system with a distribution that is essentially bilateral between the right and left breast. Current literature agrees that the parenchyma of the breast consists of about 10 to 20 lobes, each of which has a lactiferous major duct that opens on the nipple through a little antechamber called the lactiferous sinus (see Figure 2.1). Starting at the nipple, the ductal system splits up in branches that reach the back of the breast. At the end of each branch are the lobules that produce milk. Each lobule is composed of acini that empty into the terminal ducts.

Figure 2.2 shows annotated orthogonal slices of a $3D$ MR image of a breast. These images were acquired with the patient lying on her front (i.e. prone), her arms by her side and her breasts hanging under gravitational pull in the double breast coil. In this example and in general fatty and fibroglandular tissue can easily be discriminated due to their different properties [ML05].

2.2 Tumour Segmentation

The TurtleSeg software [THA11] was used to segment the datasets which is an interactive segmentation tool designed for $3D$ medical images. A typical workflow involves having

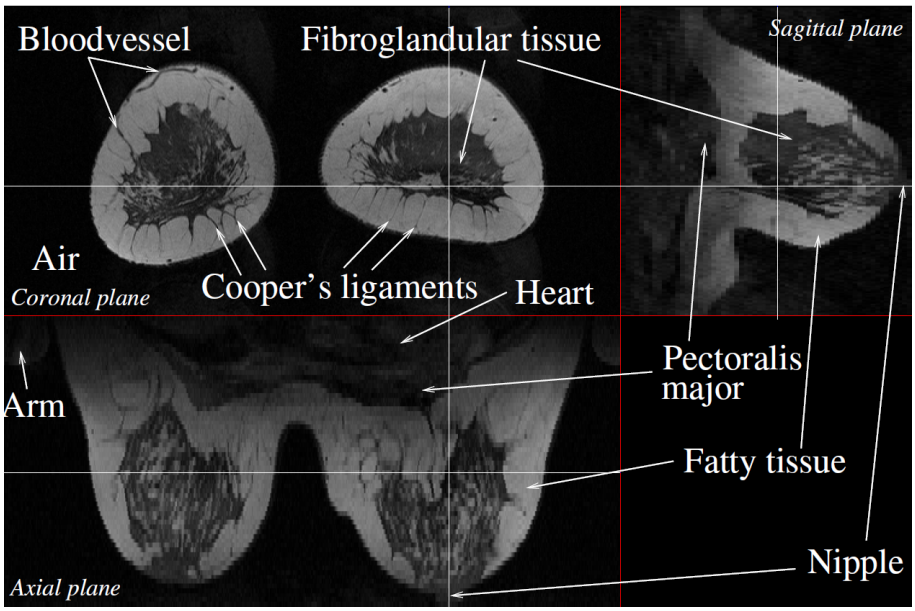

Figure 2.2: Illustration of the normal breast anatomy and its appearance on a high-resolution MR image. Tissue marked as fibroglandular includes milk ducts, glandular lobules and connective tissue as depicted in Figure 2.1.(Image is taken from [LLC09b]).

the user load a $3D$ image and then interactively contour a sparse number of different slices. The full $3D$ segmentation is then built automatically. The software has many features that will help before one starts applying matching algorithm and has automated assistance for guiding users towards better segmentations. Also, it can import and export many $3D$ file formats, including DICOM (Digital Imaging and Communications in Medicine) which is the available MRI image format in this research. The best features that specify this software in our research is to able us to export an image mask or surface mesh and then make a full contour editing support that easily allows fixing mistakes.

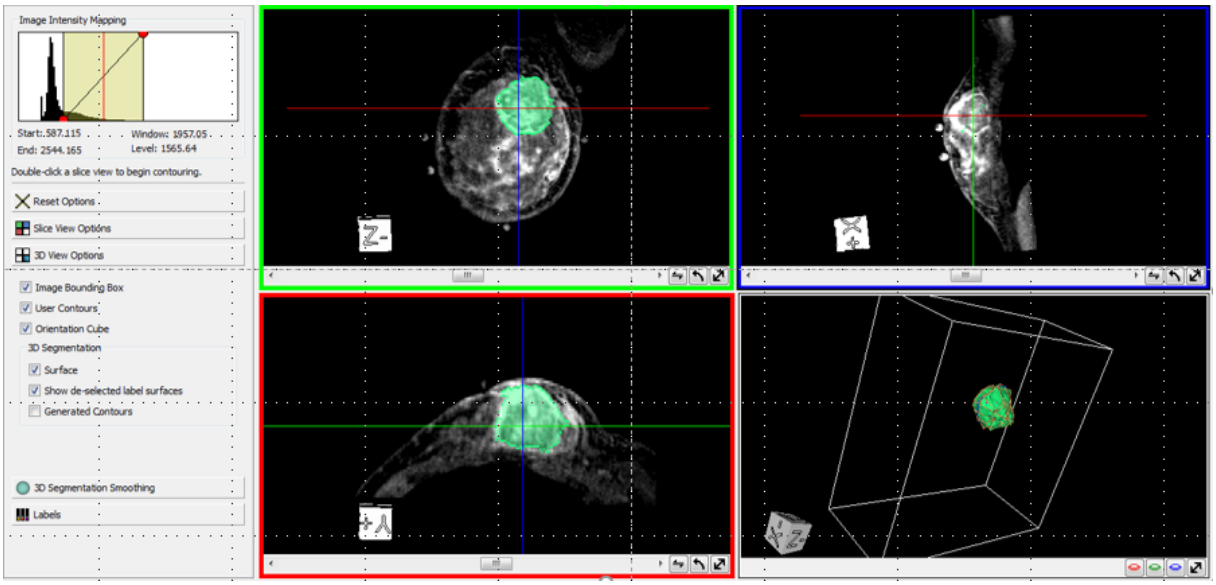

Figure 2.3: $3D$ tumour segmentation of patient no.1 (arm up position) using TurtleSeg software.

Overall, this type of segmentation enables us to separate the tumour of the breast from the surface then contour it semi-manually and use it to build the $3D$ tumour segmentation of datasets. The dataset is also exported in DICOM image format. Next, the data is exported as a mesh in a `.vtk` file format and can save as mesh files for further processing. Figure 2.3 shows semi-automatic segmentation of tumours.

Chapter 3

Preliminary Notes

3.1 Software

MATLAB[1] was chosen for implementation due to its simplicity, its arsenal of built-in functions and image viewing tools, and handy debugging tools . Although not the fastest or most efficient language (compared to C, for example), MATLAB is geared toward mathematical applications so one can write technical code in a straightforward manner without having to deal with the intricacies of programming in a language like C. Because this project focuses on the mathematical modelling aspects of image registration, speed and efficient use of computational resources were not top priority.

TurtleSeg software was used to segment the tumour in patient datasets. It is an interactive $3D$ image segmentation tool designed for $3D$ medical images [THA11]. TurtleSeg

[1] 2016 The MathWorks, Inc. MATLAB and Simulink are registered trademarks of The MathWorks, Inc. See mathworks.com/trademarks for a list of additional trademarks. Other product or brand names may be trademarks or registered trademarks of their respective holders.

implements techniques that allow the user to provide intuitive yet minimal interaction for guiding the $3D$ segmentation process.

Another Tutorial about introduction to image registration and the design of efficient and stable state of the algorithms are provided by J. Modersitzki [Mod09]. The publicly available FAIR toolbox which enables easy access to even complex schemes are the main source in the image registration researches. It is because the tutorial enables participants to use the software, explore existing registration techniques, and to design and develop new solutions. Jan Modersitzki [Mod09] also has an accompanying book of the same name that documents the code. To avoid re-inventing the wheel, our codes are written as an add-on to FAIR, keeping a similar workflow and using FAIR code whenever possible.

Another application which is called MeVisLab was chosen since it is a cross-platform application framework for medical image processing and visualization. It has some features, for instance, $2D$ image viewing and volume rendering. Furthermore, DICOM format is supported via an import to this application.

3.2 The Gaussian Mixture Model

In 1738, eighty five years after the correspondence between Pierre de Fermat and Blaise Pascal, through which the groundwork of theory was developed, the French mathematician Abraham de Moivre published the second edition of his "The Doctrine of Chances," [DM56].

It included a theorem with the first appearance of the normal probability law. However, De Moivre failed to recognize its importance as a probability density function and thus did not realize that he actually formulated what was later going to be one of the most famous formulas in the history of science [Sti86]. It was not until 1809, when Carl Friedrich Gauss introduced the concept of the normal distribution which is also called the Gaussian distribution, after him. However, the normal distribution took the form used in modern literature with the contributions of P. S. Laplace, K. Pearson and R. A. Fisher. Karl Pearson, besides his many other contributions to mathematical statistics, also is the first author to model a dataset coming from two different populations crab as a mixture of two Gaussian distributions [Pea94]. Pearson suggested fitting a mixture of two univariate normal distributions to the data, initiating the development of mixture modeling. However, the complexity of the parameter estimation problem in mixture models prevented the advance of research in this area until modern computational techniques were developed. Technology have come a long way since then, and advancements in mixture modeling followed. Unlike Pearson's crabs, the Gaussian mixture model can be used for cluster analysis. Hence, in a case where $X \in \mathbb{R}^{n \times p}$ are given (p dimensional data of size n), would be interested in estimating the number of populations (also referred as groups, clusters, classes, K), and the class membership of each observation $(\hat{y}_i | X, i = 1, 2, \ldots, n; \hat{y}_i \in 1, 2, \ldots, K)$. The Gaussian mixture model, in this case, is a useful tool to the researcher by fitting a mixture

of probability density functions to the given data, thus allowing implementation of other formal statistical procedures for estimation and optimization.

Thus, a Gaussian mixture model is a probabilistic model that assuming the observations x_{ij}, $i \in \{1, 2, \ldots, n\}$, $j \in \{1, 2, \ldots, p\}$ come from a mixture of K underlying probability distributions, each corresponding to a different cluster, the mixture density is given by,

$$f(x; w, \theta) = \sum_{k=1}^{K} w_k g_k(x; \theta_k) \tag{3.1}$$

Here $w_1, \ldots, w_K$ are the mixing proportions that satisfy $0 \leq w_k \leq 1$ and $\sum_{k=1}^{K} w_k = 1$ is the vector of unknown parameters of the k^{th} component, and w_k represents the probability that an observation belongs to the k^{th} component.

The Gaussian mixture model assumes that the components of the mixture are multivariate normal, thus the density becomes,

$$f(x; \mu, \sigma) = \sum_{k=1}^{K} w_k g_k(x; \mu_k, \sigma_k) \tag{3.2}$$

The mixture components (i.e. clusters) in Figure 3.1 are ellipsoids centered at μ_k, while the covariance matrices σ_k represent other geometric characteristics of the clusters [TSM85].

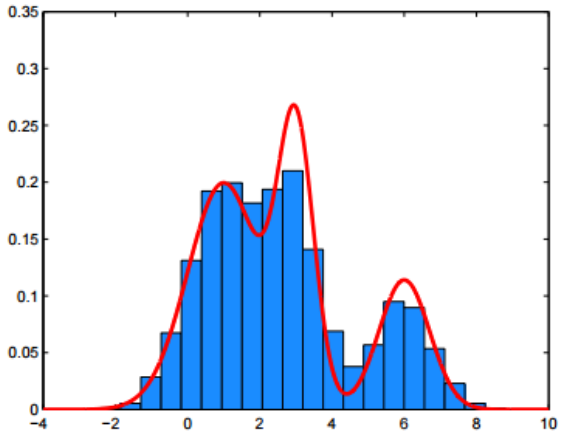

Figure 3.1: Gaussian mixture density for $K = 3$ clusters.

For instance, the component densities g_k are given by

$$g_k(x; \mu_k, \sigma_k) = \frac{1}{(2\pi)^{p/2}} \frac{w_k}{|\sigma_k|^{1/2}} \exp\left(-\frac{1}{2}(x - \mu_k)^{\mathsf{T}} \sigma_k^{-1} (x - \mu_k)\right) \tag{3.3}$$

or we can rewrite it as:

$$g_k(x; \mu_k, \sigma_k) = \frac{1}{(2\pi)^{p/2}} \frac{w_k}{|\sigma_k|^{1/2}} \exp\left(-\frac{\|x - \mu_k\|^2}{2\sigma_k^2}\right). \tag{3.4}$$

To demonstrate this, the Gaussian mixture density is fitted to a univariate dataset with $K = 3$ groups. The histogram of this data and the mixture density fit can be seen in Figure 3.1.

3.3 Parametric Transformations

Michel et al. [ZF03] presents a literature survey of automatic $3D$ surface registration techniques and mentions red that surface registration can be categories into three subjects:

1. Choice of transformation;
2. Elaboration of surface representation and similarity criterion;
3. Matching and global optimization.

The motivation of this mentioned paper is to provide a detailed overview of surface registration techniques which can be applied to the anatomical surfaces. Furthermore, the paper presents the assumptions about the type of relation between the two $3D$ surfaces which is appropriate for mapping two point sets. There are three categories:

1. Rigid-body transformation;
2. Affine transformation;
3. Non-rigid transformation.

Various parametric transformations on a point $x = (x^1, x^2)^\mathsf{T} \in \mathbb{R}^2$ or $x = (x^1, x^2, x^3)^\mathsf{T} \in \mathbb{R}^3$ are defined in this section. Each transformation is parameterized by w. Superscripts $1, 2,$ and 3 each relate to the x, y, and z coordinates in the Cartesian coordinate system, respectively.

3.3.1 Rigid Transformation

As I mentioned above, a general form of rigid body transformation can be expressed as combination of a rotation and a translation.

- **2D Rigid:** In $2D$, w contains 3 parameters: 1 rotation (w_1) and 2 translations ($w_2; w_3$). (Some conventions may refer to translations as shifts.) A rigid transformation on x is

$$y(w, x) = \begin{pmatrix} \cos w_1 & -\sin w_1 \\ \sin w_1 & \cos w_1 \end{pmatrix} x + \begin{pmatrix} w_2 \\ w_3 \end{pmatrix}. \tag{3.5}$$

- **2D Rigid - Inverse:** The inverse transform can be obtained by inverting the translation and then the rotation. The inverse transformation would simply involve negating the translation terms and rotating in the opposite direction:

$$\begin{aligned} x &= \begin{pmatrix} \cos(-w_1) & -\sin(-w_1) \\ \sin(-w_1) & \cos(-w_1) \end{pmatrix} \left[y - \begin{pmatrix} w_2 \\ w_3 \end{pmatrix} \right] \\ &= \begin{pmatrix} \cos(w_1) & -\sin(w_1) \\ \sin(w_1) & \cos(w_1) \end{pmatrix}^{\mathsf{T}} \left[y - \begin{pmatrix} w_2 \\ w_3 \end{pmatrix} \right]. \end{aligned} \tag{3.6}$$

- **3D Rigid:** In $3D$, the transformation consists of 3 rotations followed by 3 translations:

$$y(w, x) = R^1(w_1)R^2(w_2)R^3(w_3)x + (w_4, w_5, w_6)^{\mathsf{T}} \tag{3.7}$$

where w_4, w_5, and w_6 are translations in the x, y, and z directions, respectively. If w_1, w_2, and w_3 are angles of rotation about x, y, and z axes, rotation operations about the x, y, and z axes are defined to be

$$R^1(w_1) = \begin{pmatrix} 1 & 0 & 0 \\ 0 & \cos w_1 & -\sin w_1 \\ 0 & \sin w_1 & \cos w_1 \end{pmatrix}, \qquad R^2(w_2) = \begin{pmatrix} \cos w_2 & 0 & \sin w_2 \\ 0 & 1 & 0 \\ -\sin w_2 & 0 & \cos w_2 \end{pmatrix},$$
$$R^3(w_3) = \begin{pmatrix} \cos w_3 & -\sin w_3 & 0 \\ \sin w_3 & \cos w_3 & 0 \\ 0 & 0 & 1 \end{pmatrix}. \tag{3.8}$$

- **3D Rigid - Inverse:** For convenience, let us define the composition of the three rotations to be $R_w = R^1(w_1)R^2(w_2)R^3(w_3)$. As in the $2D$ case, if the forward transform is

$$y(w, x) = Rx + (w_4, w_5, w_6)^\mathsf{T} \tag{3.9}$$

then

$$x = R_w^{-1}\left[y - \begin{pmatrix} w_4 \\ w_5 \\ w_6 \end{pmatrix}\right] = R_w^\mathsf{T}\left[y - \begin{pmatrix} w_4 \\ w_5 \\ w_6 \end{pmatrix}\right], \tag{3.10}$$

since the matrix R_w is orthogonal.

3.3.2 Affine Transformation

The affine transformation was applied in this research. In addition to translation and rotation, an affine transformation allows for shearing and in particular, for scaling.

- **2D Affine:** In $2D$, the affine transformation is parametrized by 6 parameters $w = (w_1, w_2, \ldots, w_6)$. If we define

$$A = \begin{pmatrix} w_1 & w_2 \\ w_4 & w_5 \end{pmatrix}, \qquad b = \begin{pmatrix} w_3 \\ w_6 \end{pmatrix}, \tag{3.11}$$

  the transformation on a point $x = (x^1, x^2)^\mathsf{T}$ is $y(w, x) = Ax + b$.

- **2D Affine - Inverse:** Assuming that A is invertible, the inverse process is similar to the rigid case. We obtain $x = A^{-1}(y - b)$. In registering images of real objects, transformations are required to be realistic and physically feasible. It is safe to assume that all parametric transformations in this thesis, are physically feasible and therefore non-degenerate and invertible.

- **3D Affine:** If we define

$$A = \begin{pmatrix} w_1 & w_2 & w_3 \\ w_5 & w_6 & w_7 \\ w_9 & w_{10} & w_{11} \end{pmatrix}, \qquad b = \begin{pmatrix} w_4 \\ w_8 \\ w_{12} \end{pmatrix}, \tag{3.12}$$

then an $3D$ affine transformation on a point with coordinates $x = (x^1, x^2, x^3)^\mathsf{T}$ is defined as $y(w, x) = Ax + b$.

- **3D Affine - Inverse:** Again, assuming that the transformation A is physically feasible and therefore invertible, $x = A^{-1}(y - b)$.

The following explanation has been added regarding the different categories of the affine transformations: Suppose A and B are the two data sets that we want to map A to B using function f. As can be seen in the following Figure 3.3.2, there are three different situations:

- $f : A \to B$ is surjective (or onto) if $f(A) = B$; that is, f is surjective if every element of B is the image of at least one element of A.
- $f : A \to B$ is injective (or one-to-one) if each element in the range of f is the image of exactly one element of A; that is, f is injective if $f(x) = f(y)$ implies $x = y$.
- $f : A \to B$ is bijective if it is both surjective and injective.

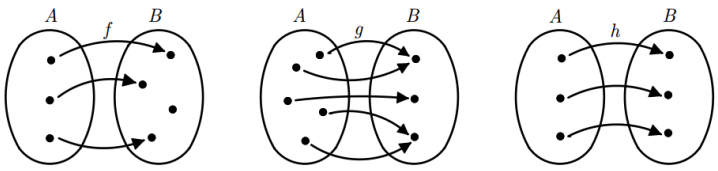

(i) f is injective (ii) g is surjective (iii) h is bijective

The above explanation shows that f has an inverse if and only if f is a bijection. Moreover, for one to one affine transformation A always has less number of elements which technically happens in many registration applications. We always want to register a point cloud with a set of guiding points.

For many applications the transformation must be one-to-one. All rigid, and almost all affine are one- to- one. Also one of the other characteristic in the affine transformation is that it does not in general preserve angles or lengths, but parallel lines remain parallel.

Maintz et al. [MvdEV96] proposed a survey paper about various types of parametric transformation. They introduced the non-rigid transformation and in addition, they expressed that the nonrigid transformation can be separated as three partitions: generalization of rigid body motion, global polynomial functions, and local non-rigid transformations. In most of the studies, rigid-body registration is mostly command. Alignments are only made by translation and rotation to match two datasets. While rigid registration is generally employed to reduce computational cost and to speed up the registration process, it risks oversimplifying the movement of body tissues, which are generally not rigid. The highly deformable nature of the breast and displacement at various positions makes registration of the breast region challenging. Registration accuracy at the millimetre scale is important during image-guided breast intervention, but is influenced by various imaging parameters. Deformable registration may be more accurate, but is computationally much more expensive.

3.4 Optimization

In registration framework, we have to iteratively minimize or maximize the cost function and update parameters. We will use the terms optimization and minimization interchangeably in this thesis, since the maximization of a function is equivalent to the minimization of the negative of the function. The function is usually called the objective function or the cost because it is the value in question we want to reduce or a penalty to be avoided.

The fact that image registration is an optimization problem benefits itself from a vast amount of literature on one of the most studied subject in mathematics. Popular optimization methods include gradient descent [NW06], conjugate gradient [Møl93], Newton type (quasi-Newton [DM77], Gauss-Newton [NW06], etc.). However, every benefit has its pay-off. The various availabilities of optimisation methods trigger two problems: the choice of optimisation methods and the parameter settings for optimisation problems. Since this measure depends on crude image values, without extracting and using any additional information, it works best on images of the same modality, i.e. images taken with the same type of imaging equipment [HM04].

In the next chapter, image registration is introduced as a minimization problem by introducing the Coherent Point Drift algorithm and various issues surrounding it will be discussed.

3.5 Interpolation

Since the registration problem is a discretized one, interpolation is needed to compute the discrete transformed coordinates and the transformed template image.

$T(x)$ is well-defined, but for a given$w$, $y(w;x)$ likely will not coincide with gridpoints of x. Thus, $T(y(w;x))$ is technically not defined. An interpolation step is necessary to compute the transformed template image over the discrete domain. Thus, the registration problem is a highly non-linear one and a closed-form solution can not be found. For this reason we must numerically optimize the problem to find a solution. For simplicity, a linear interpolator will be used for registration experiments presented in this thesis.

Linear interpolation is a reasonable tool in image registration. The interpolant can be evaluated with low computational costs and has attractive features. For example, the values of the interpolant do not exceed the interval spanned by the data, and the interpolation

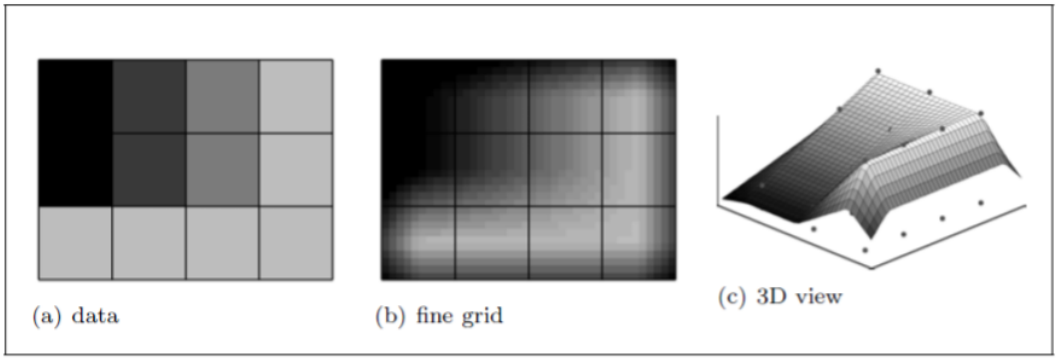

Figure 3.2: Linear interpolation (it is taken from [Mod09]).

has no spurious oscillations. However, although the interpolant is differentiable almost everywhere, it is not differentiable at the grid points. Linear interpolation is thus the interpolation method of choice when no derivatives are needed. In order to benefit from fast and efficient optimization schemes, smoother interpolants are needed.

Chapter 4

Materials and Methods

4.1 Coherent Point Drift (CPD) Registration Algorithm

In this section, a description of the CPD landmark-based registration is presented. Originally introduced by Myronenko et al. [MSCP06], the proposed method is a true probabilistic approach and is shown to be accurate and robust in the presence of outliers and missing points, and is effective for estimation of complex non-linear deformable transformations.

A few basic equalities that are often used during the explanation of the CPD algorithm are

- Conditional probabilities

$$p(A \cap B) = p(A|B)p(B), \tag{4.1}$$

- Bayes' rule

$$p(B|A) = \frac{p(A|B)p(B)}{P(A)}, \tag{4.2}$$

- if $\bigcup_{i=1}^{K} B_i = \Omega$ and $\forall i \neq j : B_i \cap B_j = \emptyset$ then

$$p(A) = \sum_{i=1}^{K} p(A \cap B_i). \tag{4.3}$$

4.1.1 Gaussian Mixture Model

The method begins with a template set of points $Y = (\mathbf{y}_1, \mathbf{y}_2, \ldots, \mathbf{y}_M)^\mathsf{T}$ where each $\mathbf{y}_i \in \mathbb{R}^d$. In practice, Y can be treated as a matrix in $\mathbb{R}^{M \times d}$. Using Y, one can create a Gaussian mixture model with the $\mathbf{y}_i$ acting as the mean values. To be precise, if Z is the random variable denoting position then given the jth element of Y, Z is distributed as a Gaussian with mean $\mathbf{y}_j$ and covariance C_j. If we further denote the probability of choosing the jth element of Y as $0 \leq w_j \leq 1$ then conditioning on j,

$$\begin{aligned} P(Z = \mathbf{z}; Y) &= \sum_{j=1}^{M} P(Z = \mathbf{z}|\mathbf{y}_j)P(j) \\ &= \frac{1}{(2\pi)^{d/2}} \sum_{j=1}^{M} \frac{w_j}{(\det C_j)^{1/2}} \exp\left(-(\mathbf{z} - \mathbf{y}_j)^\mathsf{T} \frac{\mathbb{C}_j^{-1}}{2} (\mathbf{z} - \mathbf{y}_j) \right). \end{aligned} \tag{4.4}$$

If we assume an isotropic covariance common to all the points then $C_j = \sigma^2 \mathbf{I}_d$ and the points are all equally likely then $w_j = \frac{1}{M}$, simplifies (4.4) to[1]

$$P(Z = \mathbf{z}; Y) = \frac{1}{(2\pi\sigma^2)^{d/2} M} \sum_{j=1}^{M} \mathrm{e}^{-\frac{1}{2\sigma^2}\|\mathbf{z}-\mathbf{y}_j\|_2^2}. \tag{4.5}$$

Using this induced probability distribution, we consider likelihood, $\mathcal{L}$, of an independent reference set $X = (\mathbf{x}_1, \mathbf{x}_2, \ldots, \mathbf{x}_N)^{\mathsf{T}}$ with each $\mathbf{x}_i \in \mathbb{R}^d$. In the case of (4.5), this is given as

$$\begin{aligned} \mathcal{L} = P(\mathbf{x}_1, \mathbf{x}_2, \ldots, \mathbf{x}_N) &= P(\mathbf{x}_1) P(\mathbf{x}_2) \cdots P(\mathbf{x}_N) \\ &= \frac{1}{(2\pi\sigma^2)^{d/2} M} \prod_{i=1}^{N} \sum_{j=1}^{M} \mathrm{e}^{-\frac{1}{2\sigma^2}\|\mathbf{x}_i-\mathbf{y}_j\|_2^2} \end{aligned} \tag{4.6a}$$

and taking the logarithm of the likelihood function one has

$$\log \mathcal{L} = \sum_{i=1}^{N} \log \left(\sum_{j=1}^{M} \exp\left(-\frac{1}{2\sigma^2} \|\mathbf{x}_i - \mathbf{y}_j\|_2^2 \right) \right) - \frac{d}{2} \log 2\pi - d \log \sigma - \log M. \tag{4.6b}$$

Since only the first term is relevant to characterize the likelihood of X, the other terms were removed from (4.6b) and obtained

$$\mathcal{G} = g_{N,M}(X; Y) = \sum_{i=1}^{N} \log \left(\sum_{j=1}^{M} \exp\left(-\frac{1}{2\sigma^2} \|\mathbf{x}_i - \mathbf{y}_j\|_2^2 \right) \right) \tag{4.7}$$

[1] $\|\cdot\|_2$ denotes the Euclidean norm in $\ell^2(\mathbb{R}^d)$.

measures the likelihood of X given that Y determine the mean locations of an underlying Gaussian mixture model.

Limiting cases

To get an impression of the operation of $g_{N,M}$, consider the two extremes: (i) Y consists of a single value that governs the placement of N elements of X and (ii) Y has a full complement of M values that provide influence to place a single $\mathbf{x}_1$. In the former,

$$g_{N,1} = -\frac{1}{2\sigma^2}\sum_{i=1}^{N}\|\mathbf{x}_i - \mathbf{y}_1\|_2^2 \tag{4.8a}$$

is maximized if $\mathbf{x}_i = \mathbf{y}_1, \forall i$. In the latter case,

$$g_{1,M} = \log\left(\sum_{j=1}^{M}\exp\left(-\frac{1}{2\sigma^2}\|\mathbf{x}_1 - \mathbf{y}_j\|_2^2\right)\right) \tag{4.8b}$$

for which $\mathbf{x}_1$ is chosen so that[2]

$$\mathbf{x}_1\sum_{j=1}^{M}\exp\left(-\frac{1}{2\sigma^2}\|\mathbf{x}_1 - \mathbf{y}_j\|_2^2\right) = \sum_{j=1}^{M}\mathbf{y}_j\exp\left(-\frac{1}{2\sigma^2}\|\mathbf{x}_1 - \mathbf{y}_j\|_2^2\right) \tag{4.8c}$$

showing that $\mathbf{x}_1$ is the self consistent expected value of the $\mathbf{y} \in Y$ taking into account the probability that it induces. Some caution is required for $\sigma \ll 1$ when $N \ll M$, which is

[2]Note that $\nabla_{\mathbf{x}}\|\mathbf{x} - \mathbf{y}_j\|_2 = (\mathbf{x} - \mathbf{y}_j)\|\mathbf{x} - \mathbf{y}_j\|_2^{-1}$.

illustrated in the following example. Let $Y = \{-1, 0, 1\}$ and consider

$$g_{1,3}(x;\sigma) = \log\left(\exp\left(-\frac{1}{2\sigma^2}|x+1|^2\right) + \exp\left(-\frac{1}{2\sigma^2}|x|^2\right) + \exp\left(-\frac{1}{2\sigma^2}|x-1|^2\right)\right). \tag{4.8d}$$

It is easy to verify that this has a local maximum at $x = 0$, and provided σ is sufficiently small, additional local maximum at $x = \pm 1$. However, $g(0;\sigma) = \log(1+2\mathrm{e}^{-1/2\sigma^2}) > g(\pm 1;\sigma) = \log(1+\mathrm{e}^{-1/2\sigma^2}+\mathrm{e}^{-2/\sigma^2})$ so the maximum is attained at $x_1 = 0$ but $\lim_{\sigma\to 0}|g(0;\sigma) - g(\pm 1;\sigma)| = 0$.

4.1.2 Map Smoothness

In mathematical analysis, the smoothness of a function is a property measured by the number of derivatives it has which are continuous. A smooth function is a function that has derivatives of all orders everywhere in its domain.

The function f is said to be of class C^∞, or smooth, if it has derivatives of all orders. The function f is said to be of class C^ω, or analytic, if f is smooth and if its Taylor series expansion around any point in its domain converges to the function in some neighborhood of the point. C^ω is thus strictly contained in C^∞. To put it differently, the class C^0 consists of all continuous functions. The class C^1 consists of all differentiable functions whose derivative is continuous; such functions are called continuously differentiable. Thus,

a C^1 function is exactly a function whose derivative exists and is of class C^0.

The various order of parametric continuity can be described as follows:

- C^{-1}: curves are discontinuous;
- C^0: curves are continuous;
- C^1: first derivatives are continuous;
- C^2: first and second derivatives are continuous;
- C^n: first through n^{th} derivatives are continuous.

For CPD we suppose that the sets X and Y are connected through a map $f : \mathbb{R}^d \mapsto \mathbb{R}^d$ with X acting as a finite sample of the domain and Y an independent finite sample of the range. We also presume that each component of f (with a certain abuse of notation, denoted as f as well) is sufficiently regular, $f \in L^2(\mathbb{R}^d) \cap L^\infty(\mathbb{R}^d)$, to have a well defined Fourier transform

$$\hat{f}(\mathbf{s}) = \int_{\mathbf{R}^d} f(\mathbf{t}) \mathrm{e}^{-2\pi i \mathbf{s}\cdot\mathbf{t}} \, \mathrm{d}\mathbf{t}, \qquad \check{f}(\mathbf{t}) = \int_{\mathbf{R}^d} f(\mathbf{s}) \mathrm{e}^{2\pi i \mathbf{s}\cdot\mathbf{t}} \, \mathrm{d}\mathbf{s} \tag{4.9}$$

with its corresponding inverse transform.[3]

[3]Finding the correction inversion expression for any given definition of the Fourier transform depends primarily on the expressions $\int_{\mathbb{R}} \mathrm{e}^{is(t-t_0)} \, \mathrm{d}s = 2\pi\delta(t-t_0)$ and $\delta(at) = \frac{1}{|a|}\delta(t)$, both defined in the sense of distributions. If $\hat{f}(\mathbf{s}) = A\int_{\mathbb{R}^d} f(\mathbf{t})\mathrm{e}^{i\alpha\mathbf{s}\cdot\mathbf{t}} \, \mathrm{d}\mathbf{t}$ and $\check{f}(\mathbf{t}) = B\int_{\mathbb{R}^d} f(\mathbf{s})\mathrm{e}^{-i\alpha\mathbf{s}\cdot\mathbf{t}} \, \mathrm{d}\mathbf{s}$ then the condition that $\hat{f}\circ\check{f} = \check{f}\circ\hat{f} = \mathbf{I}_d$ is satisfied if $(2\pi)^d AB = |\alpha|^d$. Consistent with this condition is the choice $A = B = 1, \alpha = -2\pi$ used herein.

Finally, we characterize each map f by a smoothness defined as a high pass filter of the power spectrum of the function and in particular

$$\mathcal{S}(f) = \int_{\mathbf{R}^d} \frac{|\hat{f}(\mathbf{s})|^2}{\hat{G}(\mathbf{s})}\, \mathrm{d}\mathbf{s} \tag{4.10}$$

where $\hat{G}$ is the Fourier transform of some real-valued function G. We require that $\hat{G}$ is a positive real-valued function with the property that $\lim_{\|\mathbf{s}\|\to\infty} \hat{G}(\mathbf{s}) = 0$. As a result,

$$G(\mathbf{t}) = \int_{\mathbb{R}^d} \hat{G}(\mathbf{s}) e^{2\pi i \mathbf{s}\cdot\mathbf{t}}\, \mathrm{d}\mathbf{s} = \int_{\mathbb{R}^d} \hat{G}^*(\mathbf{s}) e^{-2\pi i \mathbf{s}\cdot\mathbf{t}}\, \mathrm{d}\mathbf{s} = G^*(-\mathbf{t}) = G(-\mathbf{t}) \tag{4.11}$$

and in an analogous way, $\hat{G}(\mathbf{s}) = \hat{G}^*(\mathbf{s}) = \hat{G}(-\mathbf{s})$. A particularly convenient realization is

$$G(\mathbf{t}) = \mathrm{e}^{-\frac{|\mathbf{t}|^2}{2\beta^2}}, \qquad \hat{G}(\mathbf{s}) = (2\pi\beta^2)^{d/2} \mathrm{e}^{-\frac{\beta^2}{2}|2\pi\mathbf{s}|^2}. \tag{4.12}$$

Correspondingly with this choice for $\mathcal{S}$, we can compute the effect on a single frequency component $f(\mathbf{t}) = (\sin\omega t_1, \sin\omega t_2, \ldots, \sin\omega t_d)^{\mathsf{T}}$. Although $f \notin L^2(\mathbb{R}^d)$, one can determine in the sense of distributions that[4]

$$2i\hat{f}(\mathbf{s}) = \delta\left(\mathbf{s} - \frac{\omega}{2\pi}\mathbf{1}_d\right) - \delta\left(\mathbf{s} + \frac{\omega}{2\pi}\mathbf{1}_d\right). \tag{4.13a}$$

[4]The former result follows from the filtering action of the delta function so that $\int_{\mathbb{R}} \delta(t-t_0)\mathrm{e}^{-2\pi i s t}\, \mathrm{d}t = \mathrm{e}^{-2\pi i s t_0}$, the relation $2i\sin\omega t_i = \mathrm{e}^{i\omega t_i} - \mathrm{e}^{-i\omega t_i}$, and the scaling rule that $\delta(at) = \frac{1}{|a|}\delta(t)$ for any $a \in \mathbb{R}$.

Furthermore,[5]

$$4|\hat{f}(\mathbf{s})|^2 = \delta\left(\mathbf{s} - \frac{\omega}{2\pi}\mathbf{1}_d\right) + \delta\left(\mathbf{s} + \frac{\omega}{2\pi}\mathbf{1}_d\right) \tag{4.13b}$$

and as a result

$$\mathcal{S}(f) = \left(\frac{1}{4\pi\beta^2}\mathrm{e}^{\beta^2\omega^2}\right)^{\frac{d}{2}} \tag{4.13c}$$

showing that $\mathcal{S}$ acts as a measure of frequency and in this case the frequency component is proportional to $\log \mathcal{S}$.

4.1.3 Minimization I

The dual objectives of maximizing $\mathcal{G}$ (minimizing $-\mathcal{G}$) and minimizing $\mathcal{S}$ can be attained with a linear combination

$$\mathcal{E} = -\sum_{i=1}^{N} \log\left(\sum_{j=1}^{M} \exp\left(-\frac{1}{2\sigma^2}\left\|\mathbf{x}_i - \mathbf{y}_j\right\|_2^2\right)\right) + \frac{\lambda}{2}\int_{\mathbf{R}^d} \frac{|\hat{f}(\mathbf{s})|^2}{\hat{G}(\mathbf{s})}\,\mathrm{d}\mathbf{s} \tag{4.14a}$$

for some chosen $\lambda \in \mathbb{R}$, which acts as a tradeoff parameter, and connection through the map f that

$$\mathbf{y}_j = \mathbf{y_0}_j + f(\mathbf{y_0}_j) = \mathbf{y_0}_j + \int_{\mathbf{R}^d} \hat{f}(\mathbf{s})\mathrm{e}^{2\pi i \mathbf{s}\cdot\mathbf{y_0}_j}\,\mathrm{d}\mathbf{s} \tag{4.14b}$$

[5]Using the autocorrelation functions $a(\tau) = \lim_{T\to\infty}\frac{1}{T}\int_{-T/2}^{T/2} f(t)f(t+\tau)\,\mathrm{d}t$ and the relationship that $\hat{a} = |\hat{f}|^2$. For $f(t) = \sin(\omega t)$, $a(t) = \frac{1}{2}\cos\omega t$. Taking the Fourier transform gives the result.

with $\mathbf{y_0}_j$ being an unknown pre-image of $\mathbf{y}_j$ under the action of the map. This same expression can also be found by also conditioning the likelihood on the smoothness $\mathcal{S}$ provided it takes on an exponential distribution $\frac{\lambda}{2}\mathrm{e}^{-\frac{1}{2}\lambda\mathcal{S}}$ placing a decreasing probability on increasing $\mathcal{S}$.

Before taking the variation of $\mathcal{E}$ with respect to $\hat{f}(\mathbf{t})$ we first note that since f is real-valued,

$$\hat{f}^*(\mathbf{s}) = \int_{\mathbb{R}^d} f^*(\mathbf{t}) e^{2\pi i \mathbf{s}\cdot\mathbf{t}}\, \mathrm{d}\mathbf{t} = \int_{\mathbb{R}^d} f(\mathbf{t}) e^{2\pi i \mathbf{s}\cdot\mathbf{t}}\, \mathrm{d}\mathbf{t} = \hat{f}(-\mathbf{s}). \tag{4.15}$$

Therefore, taking the first variation with respect to $\hat{f}(\mathbf{t})$,

$$\frac{\delta}{\delta\hat{f}(\mathbf{t})}|\hat{f}(\mathbf{s})|^2 = \frac{\delta}{\delta\hat{f}(\mathbf{t})}\left(\hat{f}(\mathbf{s})\hat{f}(-\mathbf{s})\right) = \delta(\mathbf{t}-\mathbf{s})\hat{f}(-\mathbf{s}) + \hat{f}(\mathbf{s})\delta(\mathbf{t}+\mathbf{s}) \tag{4.16a}$$

and

$$\frac{\delta}{\delta\hat{f}(\mathbf{t})}\frac{\lambda}{2}\int_{\mathbf{R}^d}\frac{|\hat{f}(\mathbf{s})|^2}{\hat{G}(\mathbf{s})}\, \mathrm{d}\mathbf{s} = \frac{\lambda}{2}\left(\frac{\hat{f}(-\mathbf{t})}{\hat{G}(\mathbf{t})} + \frac{\hat{f}(-\mathbf{t})}{\hat{G}(-\mathbf{t})}\right) = \lambda\frac{\hat{f}(-\mathbf{t})}{\hat{G}(\mathbf{t})}. \tag{4.16b}$$

Using these expressions gives

$$\frac{\delta\mathcal{E}}{\delta\hat{f}(\mathbf{t})} = -\sum_{i=1}^{N}\frac{\sum_{j=1}^{M}\exp\left(-\frac{1}{2\sigma^2}\left\|\mathbf{x}_i-\mathbf{y}_j\right\|_2^2\right)\frac{1}{\sigma^2}\left(\mathbf{x}_i-\mathbf{y}_j\right)\mathrm{e}^{2\pi i\mathbf{t}\cdot\mathbf{y_0}_j}}{\sum_{j=1}^{M}\exp\left(-\frac{1}{2\sigma^2}\left\|\mathbf{x}_i-\mathbf{y}_j\right\|_2^2\right)} + \lambda\frac{\hat{f}(-\mathbf{t})}{\hat{G}(\mathbf{t})} = 0 \tag{4.17}$$

as the condition for an extremum with respect to $\hat{f}$ where

$$\frac{\delta\mathbf{y}_j}{\delta\hat{f}(\mathbf{t})} = \int_{\mathbf{R}^d}\delta(\mathbf{t}-\mathbf{s})\mathrm{e}^{2\pi i\mathbf{s}\cdot\mathbf{y_0}_j}\, \mathrm{d}\mathbf{s} = \mathrm{e}^{2\pi i\mathbf{t}\cdot\mathbf{y_0}_j} \tag{4.18}$$

Rearranging (4.17) by exchanging the order of summation

$$\hat{f}(\mathbf{s}) = \hat{G}(-\mathbf{s}) \sum_{j=1}^{M} \mathbf{w}_j \mathrm{e}^{-2\pi i \mathbf{s}\cdot\mathbf{y_0}_j} = \hat{G}(\mathbf{s}) \sum_{j=1}^{M} \mathbf{w}_j \mathrm{e}^{-2\pi i \mathbf{s}\cdot\mathbf{y_0}_j} \tag{4.19a}$$

where the weights are

$$\mathbf{w}_j = \frac{1}{\lambda\sigma^2} \sum_{i=1}^{N} \frac{\exp\left(-\frac{1}{2\sigma^2}\left\|\mathbf{x}_i - \mathbf{y}_j\right\|_2^2\right)(\mathbf{x}_i - \mathbf{y}_j)}{\sum_{l=1}^{M} \exp\left(-\frac{1}{2\sigma^2}\left\|\mathbf{x}_i - \mathbf{y}_l\right\|_2^2\right)} \in \mathbb{R}^d. \tag{4.19b}$$

To find $f(\mathbf{t})$ we use the convolution theorem and the inverse Fourier transform to determine

$$\int_{\mathbb{R}^d} \left(\sum_{j=1}^{M} \mathbf{w}_j \mathrm{e}^{-2\pi i \mathbf{s}\cdot\mathbf{y_0}_j} \right) \mathrm{e}^{2\pi i \mathbf{s}\cdot\mathbf{t}} \, \mathrm{d}\mathbf{s} = \sum_{j=1}^{M} \mathbf{w}_j \int_{\mathbb{R}^d} \mathrm{e}^{2\pi i \mathbf{s}\cdot(\mathbf{t}-\mathbf{y_0}_j)} \, \mathrm{d}\mathbf{s} = \sum_{j=1}^{M} \mathbf{w}_j \delta(\mathbf{t} - \mathbf{y_0}_j) \tag{4.20}$$

so that

$$f(\mathbf{t}) = G(\mathbf{t}) * \sum_{j=1}^{M} \mathbf{w}_j \delta(\mathbf{t} - \mathbf{y_0}_j) = \int_{\mathbb{R}^d} G(\mathbf{s}) \sum_{j=1}^{M} \mathbf{w}_j \delta(\mathbf{t} - \mathbf{s} - \mathbf{y_0}_j) \, \mathrm{d}\mathbf{s} = \sum_{l=1}^{M} \mathbf{w}_l G(\mathbf{t} - \mathbf{y_0}_l). \tag{4.21}$$

Using expression (4.19)

$$\int_{\mathbf{R}^d} \frac{|\hat{f}(\mathbf{s})|^2}{\hat{G}(\mathbf{s})} \, \mathrm{d}\mathbf{s} = \sum_{k=1}^{M} \mathbf{w}_k^{\mathsf{T}} \sum_{l=1}^{M} \mathbf{w}_l \int_{\mathbf{R}^d} \hat{G}(\mathbf{s}) \mathrm{e}^{2\pi i \mathbf{s}\cdot(\mathbf{y_0}_k - \mathbf{y_0}_l)} \, \mathrm{d}\mathbf{s} = \sum_{k=1}^{M} \mathbf{w}_k^{\mathsf{T}} \sum_{l=1}^{M} \mathbf{w}_l G(\mathbf{y_0}_k - \mathbf{y_0}_l) \tag{4.22}$$

and together with (4.21), the objective (4.14) is minimized to

$$\mathcal{E} = -\sum_{i=1}^{N} \log \left(\sum_{j=1}^{M} \mathrm{e}^{-\frac{1}{2\sigma^2}\left\|\mathbf{x}_i - \mathbf{y}_{\mathbf{o}_j} - \sum_{l=1}^{M} \mathbf{w}_l G(\mathbf{y}_{\mathbf{o}_j} - \mathbf{y}_{\mathbf{o}_l})\right\|_2^2} \right) + \frac{\lambda}{2} \sum_{k=1}^{M} \mathbf{w}_k^{\mathsf{T}} \sum_{l=1}^{M} \mathbf{w}_l G(\mathbf{y}_{\mathbf{o}_k} - \mathbf{y}_{\mathbf{o}_l}). \tag{4.23}$$

4.1.4 Minimization II

Having minimized with respect the map we now minimize over $\{\mathbf{w}_k\}$ and this is facilitated by first defining the following matrices

$$\mathsf{W} = (\mathbf{w}_1, \mathbf{w}_2, \ldots, \mathbf{w}_M)^{\mathsf{T}} \in \mathbb{R}^{M \times d}, \qquad \mathsf{G} \in \mathbb{R}^{M \times M} : [\mathsf{G}]_{kl} = g_{kl} = G(\mathbf{y}_{\mathbf{o}_k} - \mathbf{y}_{\mathbf{o}_l}), \tag{4.24}$$

so that with this notation,

$$\begin{aligned} \sum_{k=1}^{M} \mathbf{w}_k^{\mathsf{T}} \sum_{l=1}^{M} \mathbf{w}_l G(\mathbf{y}_{\mathbf{o}_k} - \mathbf{y}_{\mathbf{o}_l}) &= \sum_{k=1}^{M} \sum_{l=1}^{M} \sum_{j=1}^{d} w_{jk} w_{lj} g_{kl} \\ &= \sum_{j=1}^{d} \sum_{k=1}^{M} w_{jk} \left(\sum_{l=1}^{M} g_{kl} w_{lj} \right) = \mathrm{Tr}\left(\mathsf{W}^{\mathsf{T}} \mathsf{G} \mathsf{W}\right). \end{aligned} \tag{4.25}$$

If we also denote

$$\mathsf{P} \in \mathbb{R}^{M \times N} : [\mathsf{P}]_{ji} = p_{ji} = \frac{\exp\left(-\frac{1}{2\sigma^2}\left\|\mathbf{x}_i - \mathbf{y}_j\right\|_2^2\right)}{\sum_{l=1}^{M} \exp\left(-\frac{1}{2\sigma^2}\left\|\mathbf{x}_i - \mathbf{y}_l\right\|_2^2\right)} \tag{4.26}$$

then[6] from (4.25)

$$\frac{\partial \mathcal{F}}{\partial \mathsf{W}} = \frac{1}{2\sigma^2} \sum_{i=1}^{N} \sum_{j=1}^{M} p_{ji} \frac{\partial}{\partial \mathsf{W}} \left(\left\| \mathbf{x}_i - \mathbf{y_0}_j - \sum_{l=1}^{M} \mathbf{w}_l G(\mathbf{y_0}_j - \mathbf{y_0}_l) \right\|_2^2 \right) + \lambda \mathsf{GW}. \tag{4.27}$$

From the definition of inner product,

$$\|\mathbf{x}_i - \mathbf{y}_j\|_2^2 = \left(\mathbf{x}_i^{\mathsf{T}} - \mathbf{y_0}_j^{\mathsf{T}} - \sum_{r=1}^{M} \mathbf{w}_r^{\mathsf{T}} G(\mathbf{y_0}_j - \mathbf{y_0}_r) \right) \left(\mathbf{x}_i - \mathbf{y_0}_j - \sum_{l=1}^{M} \mathbf{w}_l G(\mathbf{y_0}_j - \mathbf{y_0}_l) \right) \tag{4.28a}$$

and computing only those terms in (4.27) that depend on W,

$$\sum_{q=1}^{d} \sum_{i=1}^{N} \sum_{j=1}^{M} p_{ji} x_{iq} \sum_{r=1}^{M} w_{qr} g_{rj} = \sum_{q=1}^{d} \sum_{r=1}^{M} w_{qr} \sum_{j=1}^{M} g_{rj} \left(\sum_{i=1}^{N} p_{ji} x_{iq} \right) = \mathrm{Tr}(\mathsf{W}^{\mathsf{T}} \mathsf{G} \mathsf{P} X), \tag{4.28b}$$

$$\sum_{q=1}^{d} \sum_{i=1}^{N} \sum_{j=1}^{M} p_{ji} y_{0jq} \sum_{r=1}^{M} w_{qr} g_{rj} = \sum_{q=1}^{d} \sum_{r=1}^{M} w_{qr} \sum_{j=1}^{M} g_{rj} \left(\sum_{i=1}^{N} p_{ji} y_{0jq} \right) = \mathrm{Tr}(\mathsf{W}^{\mathsf{T}} \mathsf{G}\, \mathrm{diag}(\mathsf{P}\mathbf{1}_N) Y_0) \tag{4.28c}$$

where the sum $\sum_{i=1}^{N} p_{ji} y_{0jq}$ implies that the jth row of P is summed and that this sum is applied back at row j, which is simply the jth row of the matrix $\mathrm{diag}(\mathsf{P}\mathbf{1}_N)$ with $\mathbf{1}_N =$

[6] The basic matrix calculus results used are $\frac{\partial}{\partial \mathsf{W}}(\mathsf{W}^{\mathsf{T}}\mathsf{A}) = \mathsf{A}$ and $\frac{\partial}{\partial \mathsf{W}}(\mathsf{W}^{\mathsf{T}}\mathsf{A}\mathsf{W}) = (\mathsf{A} + \mathsf{A}^{\mathsf{T}})\mathsf{W}$.

$(1, 1, \ldots, 1)^{\mathsf{T}} \in \mathbb{R}^{N\times 1}$. The last relevant sum is then

$$\sum_{q=1}^{d}\sum_{i=1}^{N}\sum_{j=1}^{M}\sum_{r=1}^{M}\sum_{l=1}^{M} p_{ji}w_{qr}g_{rj}w_{lq}g_{jl} = \sum_{q=1}^{d}\sum_{r=1}^{M} w_{qr}\sum_{j=1}^{M} g_{rj}\sum_{i=1}^{N} p_{ji}\left(\sum_{l=1}^{M} g_{jl}w_{lq}\right)$$
$$= \mathrm{Tr}(\mathsf{W}^{\mathsf{T}}\mathsf{G}\,\mathrm{diag}(\mathsf{P}\mathbf{1}_N)\mathsf{G}\mathsf{W}). \tag{4.28d}$$

Completing (4.27)

$$\frac{\partial \mathcal{F}}{\partial \mathsf{W}} = \frac{1}{2\sigma^2}\left(-2\mathsf{G}\mathsf{P}X + 2\mathsf{G}\,\mathrm{diag}(\mathsf{P}\mathbf{1}_N)Y_0 + 2\mathsf{G}\,\mathrm{diag}(\mathsf{P}\mathbf{1}_N)\mathsf{G}\mathsf{W}\right) + \lambda\mathsf{G}\mathsf{W} = 0 \tag{4.29}$$

as the extremal condition for W. Simplifying, since G is nonsingular, yields the final expression of

$$\left(\mathrm{diag}(\mathsf{P}\mathbf{1}_N)\mathsf{G} + \lambda\sigma^2\mathsf{I}\right)\mathsf{W} = \mathsf{P}X - \mathrm{diag}(\mathsf{P}\mathbf{1}_N)Y_0. \tag{4.30}$$

The matching procedure required a set of parameters. We manually tuned the parameters (Table 4.1.4) for the algorithm to yield satisfactory matching of the markers in the volunteer dataset.

Free Parameters: There are three free parameters in the method: λ, β, σ. Parameter α represents the trade-off between data fitting and smoothness regularization. Parameter β reflects the strength of interaction between points. Small values of β produce locally

Symbol	Definition	Number
N	number of effective eigenvectors/ values to approximate G)	40
β	width of Gaussian distribution	
	(same unit as template pointset; in this case pixel)	3
λ	regularization weight	28
corresp	compute correspondence vector at the end of registration	300
tol	tolerance	1e-6

Table 4.1: The CPD algorithm parameters

smooth transformation, while large values β of correspond to nearly pure translation transformation. In this research, the value of the β is around 1 (mm). The value of σ serves as a capture range for each Gaussian mixture component. Smaller σ indicates smaller and more localized capture range for each Gaussian component in the mixture model. We use deterministic annealing [UN98] for σ, starting with a large value σ and gradually reducing it according to $\sigma = \alpha\sigma$, where α is annealing rate (normally between [0.92 0.98]), so that the annealing process is slow enough for the algorithm to be robust. The gradual reducing of σ leads to a coarse-to-fine match strategy [MSCP06].

4.1.5 Limitations

- The first problem is that the similarity measure only depends on the Euclidean distance between points. In the case of a large degree of degradation, such as deformation, noise, or outliers, the closest point pairs may not be in correspondence, whereas the point pairs that have the similar neighbor structures are probably in correspon-

dence. Therefore, the contribution of each Gaussian component to the GMM is not the same. The neighborhood structure similarity of the point pairs should be introduced into the proportion of the GMM components.

- The second problem existing in CPD is the outliers W, which requires manual assignment during initialization. This requirement also limits the application of CPD. It is difficult to determine the outliers of the two point sets before registration. An improper value of W leads to an unpredictable registration result. Meanwhile, CPD uses a uniform distribution $1/M$ to treat noise and outliers. The uniform distribution should be related to the coordinate range of the data points rather than the number of data points M. For example, given two data sets with the same number of points, the point's distribution range of one data set is larger than the other. Thus, the uniform distribution of the two data sets should not be equal. As a result, even if the real outliers is assigned, a good result is still not guaranteed. Only by slight adjustment of W to make the product of W and $1/M$ model the noise and outliers appropriately. Therefore, in the CPD algorithm, W can only be called an approximate outliers ratio.

4.1.6 Summary

Starting with a set of parameters σ, λ, β and set of point $X \in \mathbb{R}^{N\times d}$, $Y_0 \in \mathbb{R}^{M\times d}$. Set $k = 0$ and compute $G(Y_0)$ according to (4.24). Then iterate the following sequence of steps

- Determine $P(X, Y_k)$ with (4.26)
- Compute W from expression (4.30)
- $k = k + 1$
- Let $Y_k = Y_0 + \mathsf{GW}$

with a stopping criteria of $\|X - Y_k\|_2^2 < \epsilon$. The final map is given by

$$f(\mathbf{t}) = \sum_{l=1}^{M} \mathbf{w}_l G(\mathbf{t} - \mathbf{y_0}_l).$$

Chapter 5

Experiments and Results

5.1 Data

Table 5.1 presents the characteristics of patient datasets in [ESM+14]. Patient no. 5 was coughing throughout the scanning procedure leading to unacceptably poor quality images in which it was impossible to delineate the tumour; the data from this patient is therefore not included in the study. (See Appendix A for Figures A.7 and A.8 which present the

Patient ID	Matrix size	Field of view (mm^3)	no. of markers arm down,up and matched	Tumor size arm down (cm^3)	Tumor size arm up (cm^3)
1	$256 \times 256 \times 66$	$180 \times 180 \times 79$	$34, 33, 33$	16.8 ± 0.4	18.0 ± 1.1
2	$256 \times 256 \times 56$	$180 \times 180 \times 84$	$40, 29, 24$	5.3 ± 0.7	6.9 ± 1.0
3	$256 \times 256 \times 66$	$180 \times 180 \times 79$	$34, 35, 34$	80.5 ± 4.1	73.8 ± 1.6
4	$256 \times 256 \times 72$	$180 \times 180 \times 86$	$24, 24, 24$	2.4 ± 0.1	2.4 ± 0.4
6	$256 \times 256 \times 46$	$180 \times 180 \times 55$	$25, 25, 25$	1.9 ± 0.2	1.5 ± 0.2

Table 5.1: Characteristics of patient datasets.

different slices of the MRI for patient no. 5 when the arm adjacent to the body of the patient (reference) and the arm placed above the head of the patient, respectively.) Thus, the mentioned figures show that the location and size of the tumour in this dataset is not obvious for segmentation process. Furthermore, we only use the location information of the landmarks in the pre-surgical image and the corresponding locations during the surgery. Therefore, no image intensity information is required in the registration procedure. Figures 5.1 and 5.2 present the location of the tumour for patient no. 1 when the patient's arm adjacent to the body (supine arm down) or placed above the head (supine arm up). (Appendix A provides the location of the tumour for patient no. 2 (A.1, A.2), 3 (A.3, A.4), 4 (A.5, A.6), 5 (A.7, A.8), and 6 (A.9, A.10) when the patient's arm adjacent to the body (supine arm down) or placed above the head (supine arm up)).

Also, the different $3D$ views of tumour in patient no. 1 are shown in Figure 5.3. (See Appendix A for patient no. 2 (A.11), 3 (A.12), 4 (A.13), 5 (A.14), 6 (A.15))[1].

5.2 Marker Selection and Matching

Immediately before imaging a range of $24 - -34$ MR visible markers (Brava-Pinpoint, Beekley, USA) were placed on the skin of the left breast in a uniform distribution for each

[1]A sagittal (also known as anteroposterior) plane is an $Y - Z$ plane, perpendicular to the ground, which separates left from right. The transverse plane or axial plane (lateral, horizontal) divides the body into cranial and caudal (head and tail) portions.

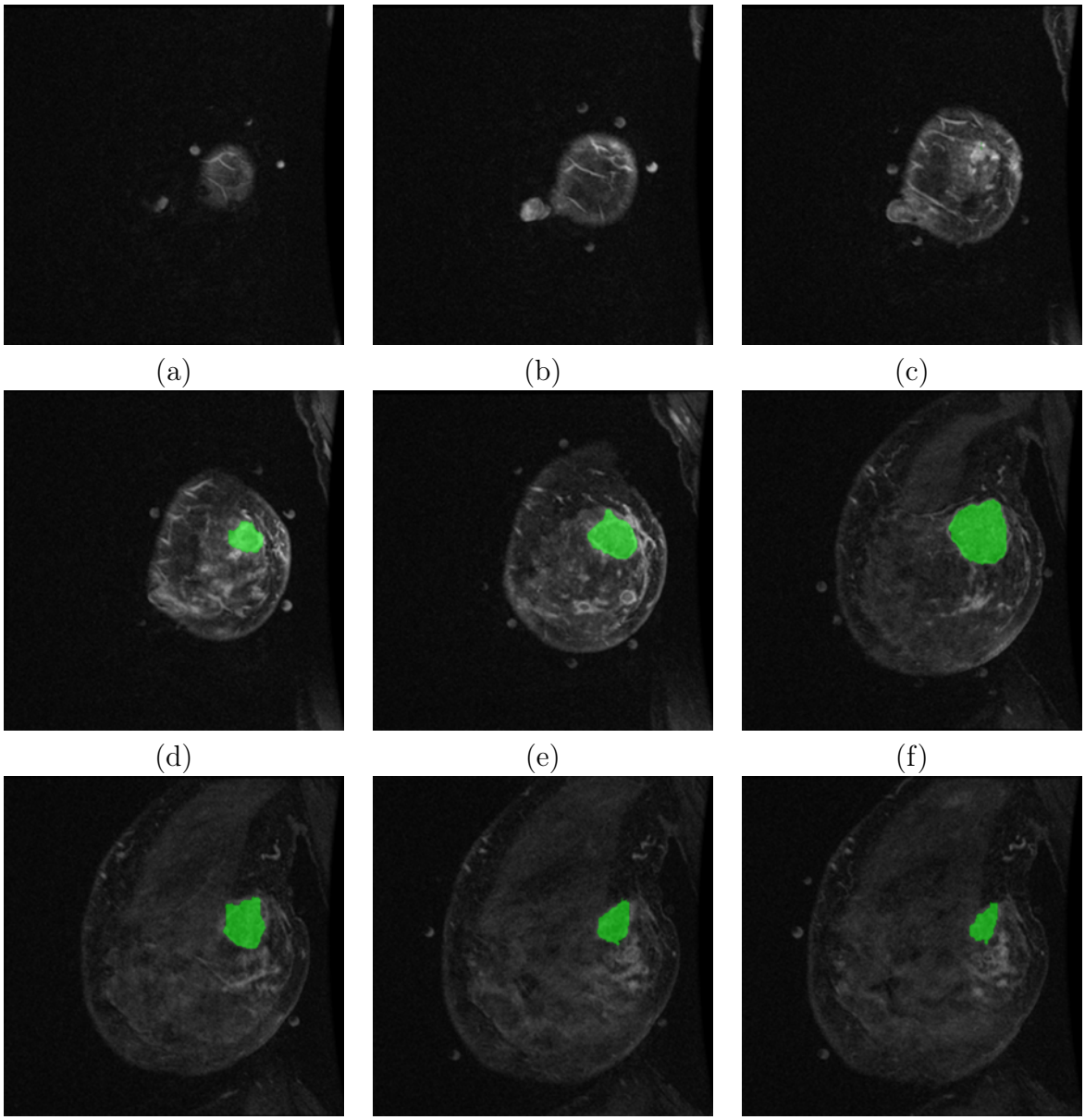

Figure 5.1: Patient no. 1; supine arm down, slice no. $10, 13, 15, 20, 30, 36, 39, 40, 45$, respectively.

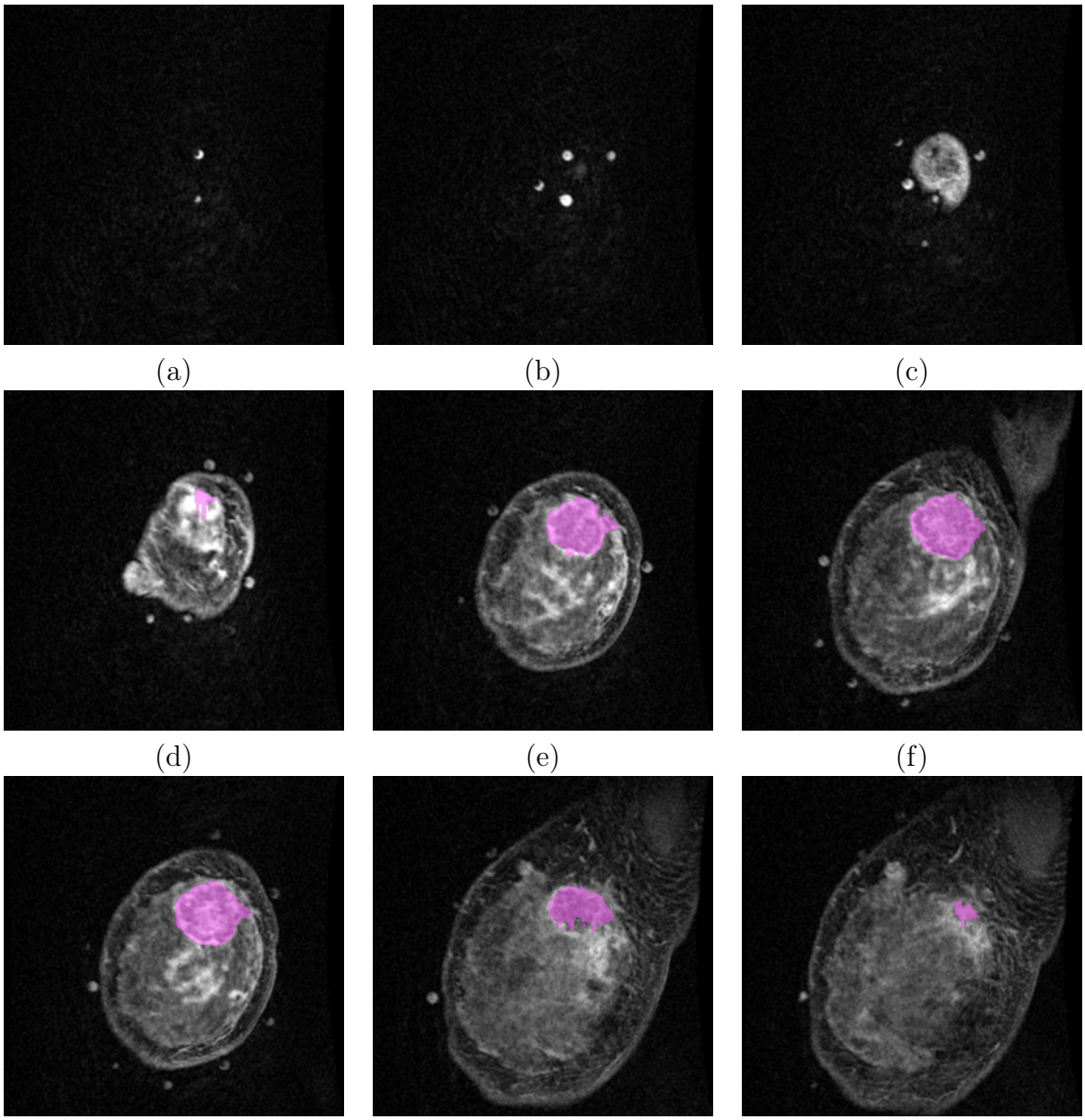

Figure 5.2: Patient no. 1; supine arm up, slice no. $10, 13, 15, 20, 30, 36, 39, 40, 45$, respectively.

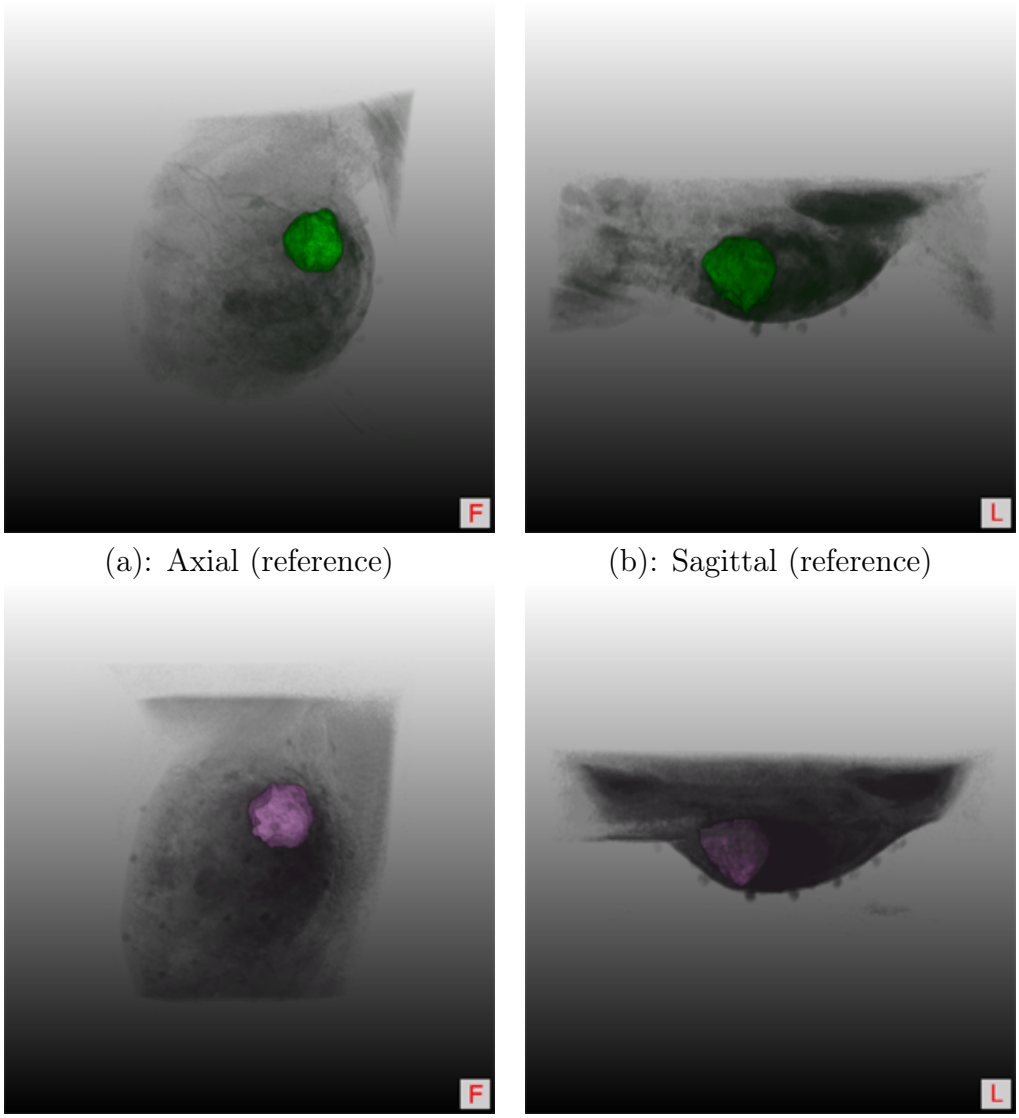

(a): Axial (reference) (b): Sagittal (reference)

(c): Axial (template) (d): Sagittal (template)

Figure 5.3: Different $3D$ views of tumour in patient no. 1.

volunteer, see Table 5.1. The markers were held with stickers to the breast skin and, in order to minimize disturbances in the natural behavior of the breast during the arm movement,

these stickers were trimmed to achieve as small a contact surface as possible [ESM+14]. Thus, the number of matched markers are presented in the fourth column of Table 5.1. It should be noted that some of the markers occasionally fell off during the process of repositioning. In addition, there is no guarantee that by moving the patient, all of the markers remain in the field of view of the image volume in the moving image compared to the fixed image. The difference between the number of markers in these two cases especially for patient no. 2 is a combined consequence of these two events.

Furthermore, the patients were initially positioned in the supine position with their arms by their sides and contrast was injected in the contralateral (right) arm. After acquiring the first contrast enhanced image the patients were then quickly repositioned for the second supine breast MRI with the arm placed above the head. The position of the MR-visible markers in the two arm-up and arm-down images for each patient were semi-manually selected and computed using a GUI tool that was developed inhouse using MATLAB [ESM+14]. The CPD registration [MS10] was then employed to match the markers for rigid, affine, and deformable transformations. The matching procedure required a set of parameters and we manually tuned the parameters for the algorithm to yield accurate matching of the markers in a volunteer dataset. In our experiments, we used the coherent point drift (CPD) package available at `sites.google.com/site/myronenko/research/cpd`. The matching procedure on the volunteer dataset was manually verified

to ensure the reliability of the tuned parameters. We then employed the same set of parameters on our patient dataset.

5.3 Tumour Segmentation

Three independent observers, all of whom were experienced in looking at breast MR images, segmented the tumours of each of the patients using TurtleSeg (Interactive $3D$ Image Segmentation Software) [THA11] that provides a semi-manual tool for segmentation. Table 5.1 summarizes the mean $\pm$ standard deviation of the segmented tumour volumes. The tumour of patient no. 3 could not be reliably identified and segmented even with the help of a radiologist therefore we segmented an enhancing cyst that was clearly visible in the images instead. Figure A.3 is shown the slice no. $10, 15, 18, 20, 30, 40$ of patient no. 3. As it shows, there is no tumour that can identify and only the cyst in this dataset is obvious for segmentation. Here, we present data for five of the patients from our study named as patient 1, 2, 3, 4, and 6.

5.4 Results

We computed the Dice measure of overlap between the tumour in the reference and the registered arm up images presented in Table 5.4. In addition, we computed the Center of

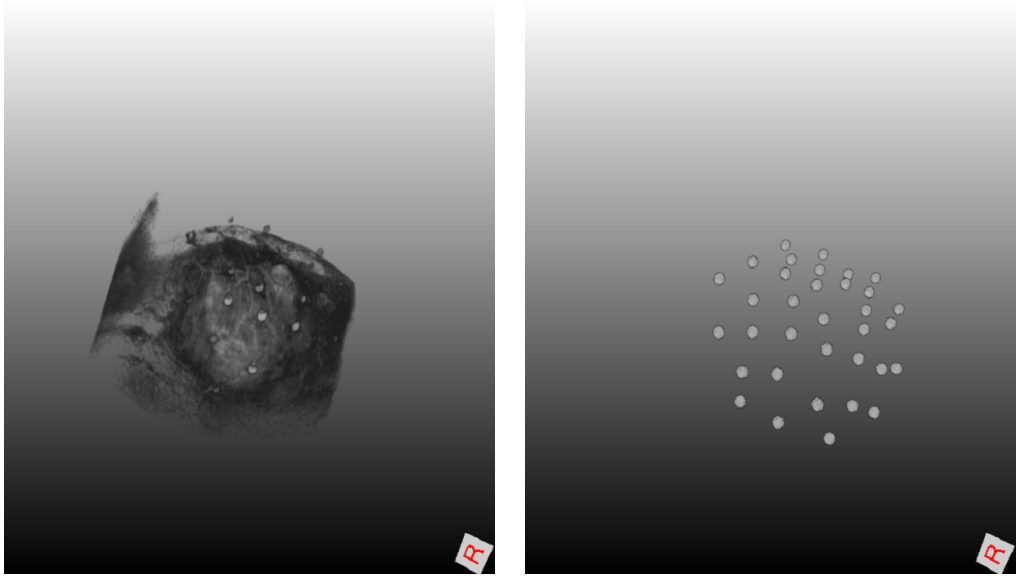

(a) (b)

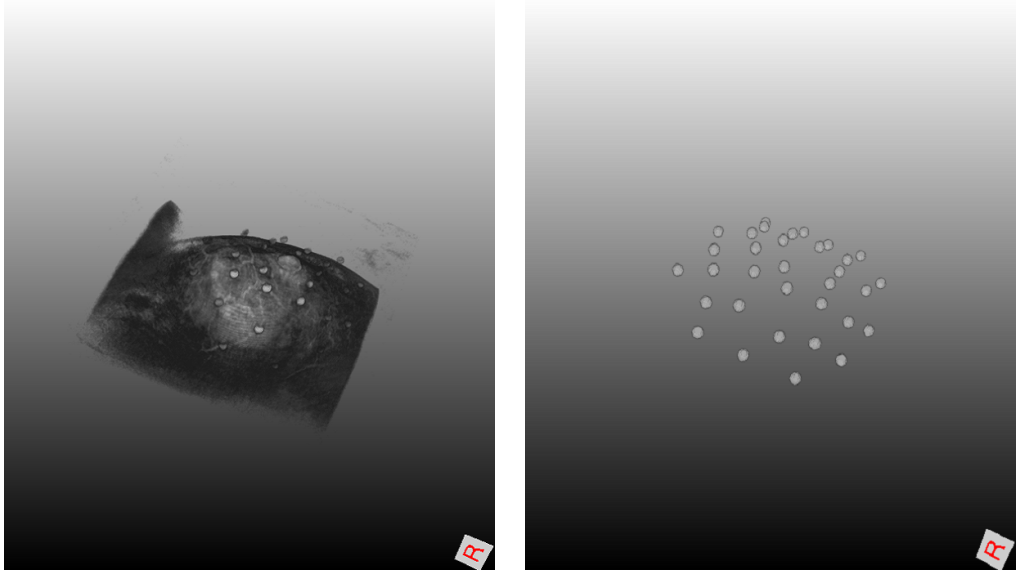

(c) (d)

Figure 5.4: Patient no. 1, showing MR visible markers in reference (arm up) and template image (arm down).

	P1 D	P1 U	P2 D	P2 U	P3 D	P3 U	P4 D	P4 U	P6 D	P6 U
Seg A and Seg B	92	86	87	82	93	92	90	75	90	86
Seg A and Seg C	93	84	83	80	93	92	87	72	81	82
Seg B and Seg C	91	88	83	80	95	89	88	77	82	84
Average	92.0	86.0	84.3	80.7	93.7	91.0	83.0	74.7	84.3	84.0

Table 5.2: Evaluating Dice measure of overlap among three tumour segmentations A, B, C, for each patient (P stand for Patient) and arm position (U and D stand for Up and Down).

	P1 D	P1 U	P2 D	P2 U	P3 D	P3 U	P4 D	P4 U	P6 D	P6 U
Seg A and Seg B	0.6	1.9	0.6	0.8	0.8	0.6	0.2	1.5	0.2	0.6
Seg A and Seg C	0.5	1.9	1.1	1.0	1.2	1.8	0.7	1.4	3.6	1.2
Seg B and Seg C	1.1	0.8	1.6	0.4	0.7	2.0	0.7	0.8	3.7	1.0
Average	0.73	1.53	1.10	0.73	0.90	1.46	0.53	1.23	2.50	0.93

Table 5.3: Evaluating COM variations among three tumour segmentations A, B, C, for each patient (P stand for Patient) and arm position (U and D stand for Up and Down) in millimeters.

Mass (COM) of the tumours and evaluated the Euclidean distance between the tumours in the reference and arm up images; this is defined as the COM-displacement Table 5.5. The focus of this study is the matching of supine breast datasets which were acquired with two different arm positions using the CPD algorithm and the positions of surface markers. Our goal was to localize the tumour using the described scheme. We used manual segmentations of the lesions to assess the Dice overlap and COM-displacement metrics.

Based on the results presented in Tables 5.4 and 5.5, it can be recognized that the deformable CPD point sets registration Dice scores were generally superior than the CPD rigid and affine except in patient 4 and 6. It can be observed that Dice measure of patient 4 was not consistent with the other patients in Table 5.4. These could be due to several factors. The initial unregistered arm-up and down positions have a displacement of 46 mm which is the largest among all of the patients in the study. Also, due to a miscommunication problem in placing the markers, only one side of the breast was covered by the markers for patient 6" [ESM+14]. In addition, the tumour is close to the COM of the markers and as expected CPD rigid gave the best results compared to CPD deformable, affine and TPS for patient 6. As we expected, the result of the experiments vary based on the tumour size, shape, and location.

One way of measuring how well images have been aligned by registration is to measure how much the template and reference images overlap before and after registration. The Dice measure is a way of quantifying the overlap between two regions. Thus, the Dice measure of overlap between the segmented breast tumour in transformed moving image (A) and the corresponding segmented breast tumour in fixed image (B) is defined as:

$$\text{Dice}(A, B) = 100 \times \frac{2|A \cap B|}{|A| + |B|}. \tag{5.1}$$

Furthermore, the center of mass (COM) variations are computed as the standard deviation

Patient ID	Unregistered	TPS registered	CPD-rigid registered	CPD-affine registered	CPD-nonrigid registered
1	(A) 28	(A) 77	(A) 65	(A) 76	(A) 78
	(B) 24	(B) 79	(B) 67	(B) 81	(B) 83
	(C) 20	(C) 74	(C) 64	(C) 76	(C) 79
2	(A) 0	(A) 75	(A) 60	(A) 72	(A) 75
	(B) 0	(B) 63	(B) 53	(B) 60	(B) 64
	(C) 0	(C) 57	(C) 52	(C) 59	(C) 64
3	(A) 26	(A) 75	(A) 79	(A) 75	(A) 85
	(B) 23	(B) 74	(B) 79	(B) 73	(B) 84
	(C) 28	(C) 77	(C) 79	(C) 76	(C) 83
4	(A) 0	(A) 20	(A) 0	(A) 20	(A) 0
	(B) 0	(B) 23	(B) 0	(B) 19	(B) 0
	(C) 0	(C) 21	(C) 0	(C) 25	(C) 0
6	(A) 6	(A) 61	(A) 81	(A) 70	(A) 72
	(B) 10	(B) 59	(B) 81	(B) 69	(B) 71
	(C) 6	(C) 59	(C) 79	(C) 70	(C) 73

Table 5.4: Dice score(%)

of the COM among these three tumour segmentations, for each patient and arm position in millimeters.

Table 5.4 evaluates the Dice measures of tumour overlap, and Table 5.5 indicates COM-displacement of tumours in millimeters before and after registration. Three values in each cell represent the values calculated based on each of the three independent tumour segmentations. The maximum possible number of available matched markers have been

Patient ID	Unregistered	TPS registered	CPD-rigid registered	CPD-affine registered	CPD-nonrigid registered
1	(A) 17.5	(A) 2.7	(A) 6.5	(A) 3.2	(A) 2.5
	(B) 18.5	(B) 3.0	(B) 6.5	(B) 3.1	(B) 2.5
	(C) 19.5	(C) 4.0	(C) 7.4	(C) 4.1	(C) 3.6
2	(A) 33.0	(A) 0.9	(A) 6.2	(A) 2.8	(A) 3.1
	(B) 33.1	(B) 1.5	(B) 7.3	(B) 2.8	(B) 3.6
	(C) 32.0	(C) 2.2	(C) 7.3	(C) 2.4	(C) 2.5
3	(A) 31.6	(A) 9.0	(A) 4.7	(A) 9.8	(A) 4.0
	(B) 32.2	(B) 9.3	(B) 4.8	(B) 10.3	(B) 4.1
	(C) 30.3	(C) 7.9	(C) 4.5	(C) 9.0	(C) 4.2
4	(A) 46.8	(A) 8.5	(A) 21.0	(A) 10.6	(A) 17.6
	(B) 46.7	(B) 8.3	(B) 23.7	(B) 10.2	(B) 19.6
	(C) 46.1	(C) 8.5	(C) 21.0	(C) 10.0	(C) 17.7
6	(A) 11.0	(A) 3.9	(A) 1.2	(A) 2.8	(A) 2.5
	(B) 10.9	(B) 4.2	(B) 1.2	(B) 3.0	(B) 2.6
	(C) 11.2	(C) 5.2	(C) 3.4	(C) 2.3	(C) 2.4

Table 5.5: COM-displacement (mm)

used for each patient. Figures 5.6 and 5.5 present the ovelap between the tumours before and after applying the CPD registration methods for patient no. 1; Slice 34 of the $3D$ volume, respectively (See Appendix A for patients no. 2 (A.17, A.16), 3 (A.19, A.18), 6 (A.21, A.20)

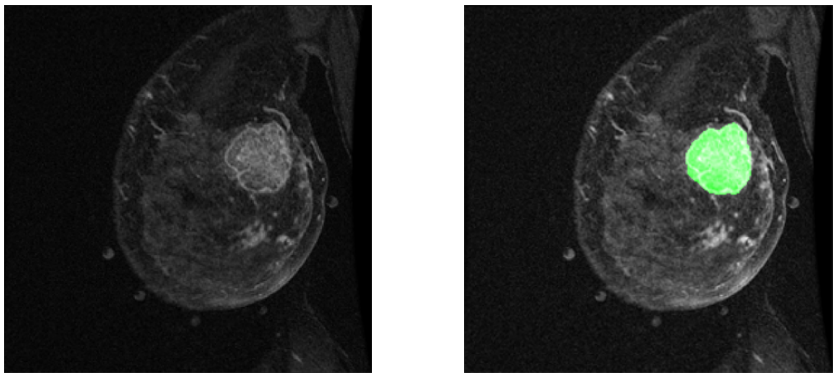

(a) Reference (arm parallel) (b) Segmented tumour in reference

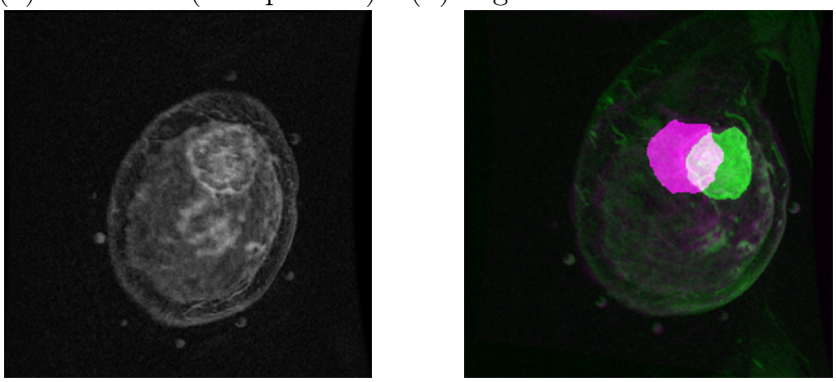

(c) Template (arm up) (d) Template overlay on reference

Figure 5.5: Patient no. 1 (Before Registration); Slice 34 of the $3D$ volume.

5.5 Computational Time

The CPD registration results reported in this paper took 0.4 to 0.6 seconds of CPU time on a 64-bit Lenovo S30 ThinkStation with a 3.7 GHz Intel Xeon E5-1620 v2 processor, running MATLAB, which is significantly lower than the computation time using TPS (under a minute) reported in [ESM+14]. In addition, Figures 5.7, 5.8, 5.9, 5.10, 5.11 represent the CPD computational time for different types of transformations (rigid, affine,

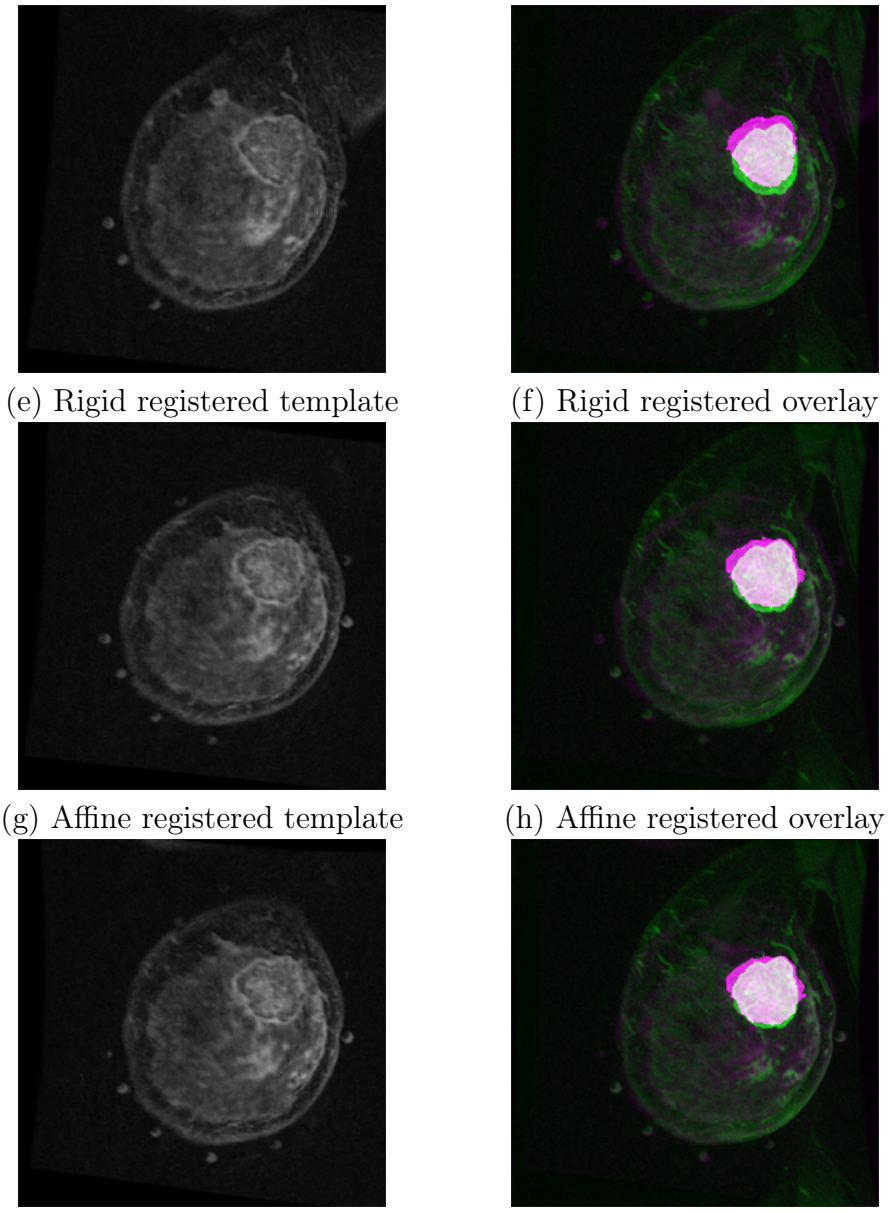

(e) Rigid registered template (f) Rigid registered overlay

(g) Affine registered template (h) Affine registered overlay

(i) Deformable registered template (j) Deformable registered overlay

Figure 5.6: The CPD rigid, affine and deformable registration for patient no. 1; Slice 34 of the $3D$ volume.

and nonrigid). As they illustrate, the running time for each of the transformations are increased by increasing the number of markers.

Furthermore, the computational complexity of CPD is $O(M^3)$, where M is the number of points in template point set [MSCP06]. Thus, The plots provide the slope of each of the transformation lines to compare with the computational complexity of the CPD. The slopes are shown as α, are between 2.99 to 3.8. The perfect computational complexity is occurred when α is 3.

Also, the Figures 5.7, 5.8, 5.9, 5.10, 5.11 show that the CPD non-rigid computational time has the higher computational time in comparing with the CPD affine and rigid for all the datasets since the complexity of the CPD algorithm for non-rigid transformation is more than the affine and rigid. In other words, finding the correct correspondence of markers in the CPD non-rigid registration take more time than the CPD affine and rigid registrations.The most rapid convergence occurs with the CPD rigid algorithm since it only involves translation and rotation.

In order to further assess the feasibility of the registration approach in a surgical setting, more volunteer patient datasets with tumours will be required.

Each registration took under 0.5 seconds to reconstruct the registered volume in MATLAB. This is important since, for the image-aided BCS, the tracking of the marker positions in the OR (Operation Room) and the registration of the supine breast MRI to the OR will

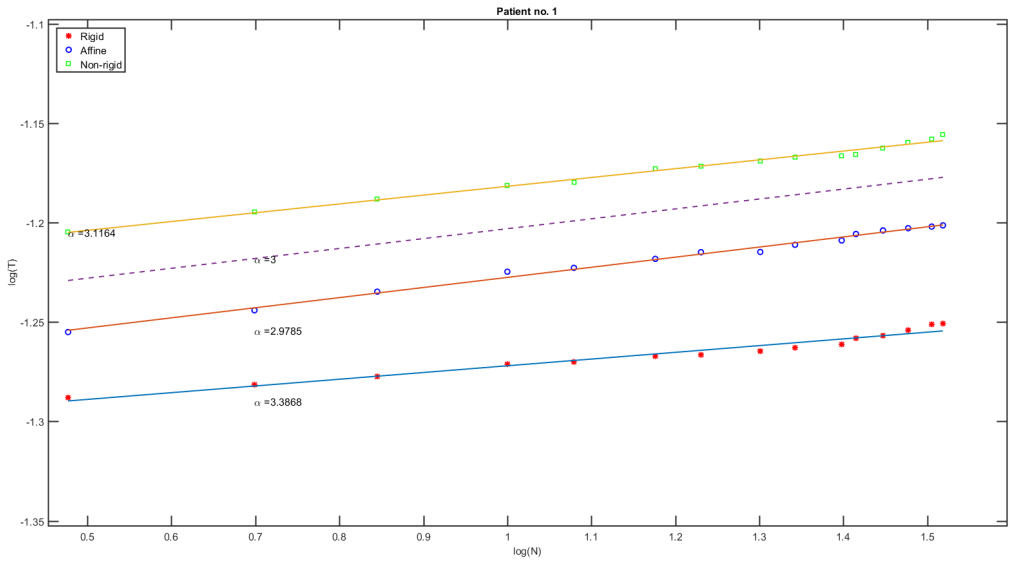

Figure 5.7: The CPD rigid, affine and deformable computational time for patient no. 1.

be done while the patient is under anesthesia therefore the registration should be carried out as quickly as possible. An implementation of the CPD algorithm in C could further improve the time efficiency. The speed of the CPD algorithm compared to TPS [ESM+14], is an important factor for the clinical application. Another reason to use CPD registration is its simplicity. In general, bio-mechanical models can lead to more accurate tumour localization and can yield superior information about tumour's shape while being more complicated to implement, see [PBSS00] as an example.

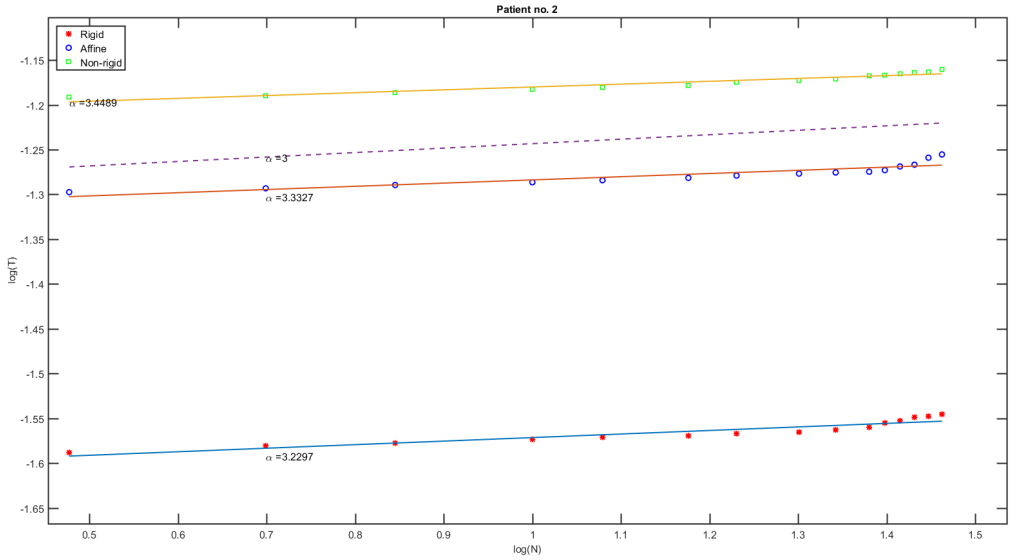

Figure 5.8: The CPD rigid, affine and deformable computational time for patient no. 2.

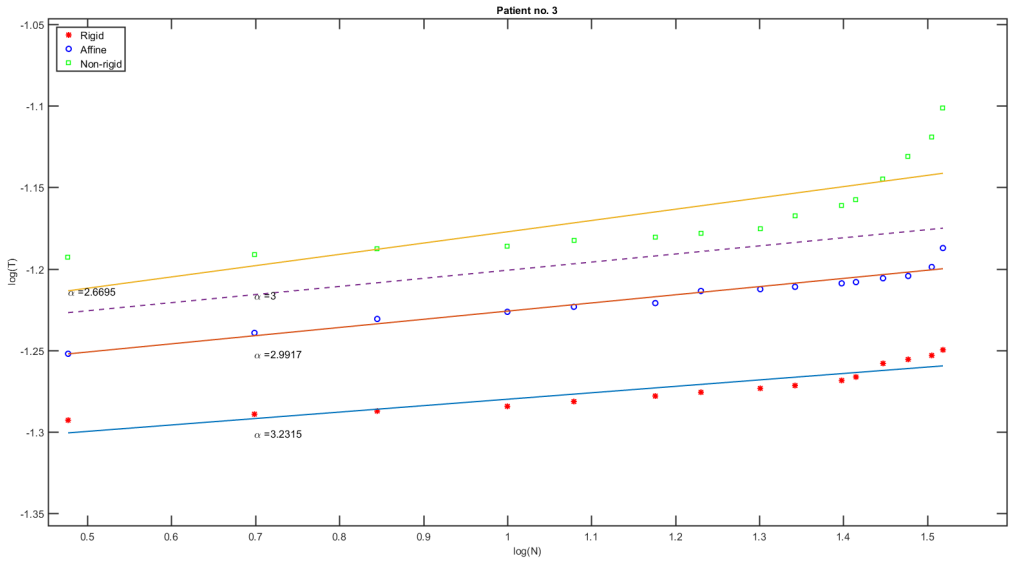

Figure 5.9: The CPD rigid, affine and deformable computational time for patient no. 3.

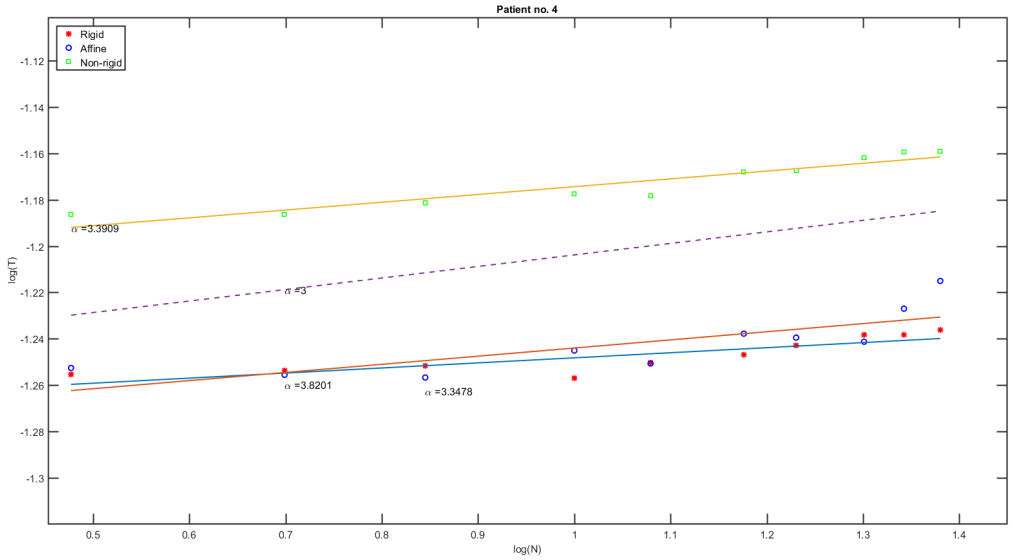

Figure 5.10: The CPD rigid, affine and deformable computational time for patient no. 4.

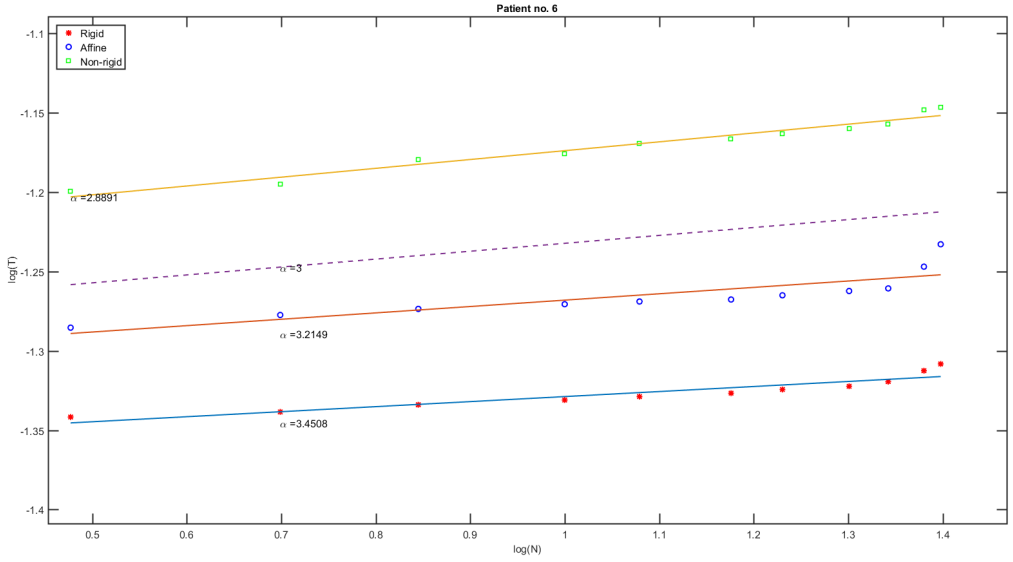

Figure 5.11: The CPD rigid, affine and deformable computational time for patient no. 6.

Chapter 6

Conclusion and Future work

6.1 Conclusion and Discussion

We apply Coherent Point Drift, a probabilistic method for rigid, affine, and non-rigid registration of two point sets. The registration is considered as a Maximum Likelihood estimation problem, where one point set represents centroids of a GMM and the other represents the data. We regularize the velocity field over the points domain to enforce coherent motion and define the mathematical formulation of this constraint. We derive the solution for the penalized ML estimation through the variational approach, and show that the final transformation has an elegant kernel form. We also derive the EM optimization algorithm with deterministic annealing. The estimated velocity field represents the underlying rigid, affine and non-rigid transformation. Once we have the final positions of

the GMM centroids, the correspondence between the two point sets can be easily inferred through the posterior probability of the GMM components given the data. The computational complexity of CPD is $O(M^3)$, where M is the number of points in template point set [MSCP06]. It is worth mentioning that the components in the point vector are not limited to spatial coordinates. They can also represent the geometrical characteristic of an object (e.g., curvature, moments), or the features extracted from the intensity image (e.g., color, gradient).

The experimental results suggest that the deformable CPD registration of $3D$ breast MRI can perform more accurately compared to the rigid, affine and TPS registration methods. In general, the motion of the breast is nonrigid so that rigid or affine transformations are not sufficient enough to describe the motion. These preliminary results also demonstrate that in general the experiments are affected by the tumour size, shape, and location. The CPD registration results reported in this paper took 0.4 to 0.6 seconds of CPU time on a 64-bit Lenovo S30 ThinkStation with a 3.7 GHz Intel Xeon E5-1620 v2 processor, running MATLAB, which is significantly lower than the computation time using TPS (under a minute) reported in [ESM+14]. In order to further assess the feasibility of the registration approach in a surgical setting, more volunteer patient datasets with tumours will be required.

In summary we have demonstrated that the alignment of pre-surgical supine MR images

to the patient using surface markers on the breast for co-registration is feasible. For BCS, co-registering pre-surgical breast MRI data with the patient positioned as for surgery will provide information on the location, extent and size of a tumour. With data for 6 volunteers, CPD algorithm worked sufficiently well, but with large uncertainty. If more data becomes available, we would test our model again to see if similar results are observed and how consistent those observations are.

6.2 Future work

With data for 5 volunteers, our observations may generalize on matching supine-supine surface-based breast MRI via markers, but with large uncertainty. If more data becomes available, we would test our model again to see if similar results are observed and how consistent those observations are.

In addition, in registering MR images, we are most interested in aligning the boundaries of organs and the outlines of their features. Thus, the conceptual framework of freeform deformations can be more practical which allows to model flexible deformations by controlling a limited number of points, instead of considering every image pixel individually.

Appendix A

Appendix

In this section, the location of the tumour for patient no. 2, 3, 4, 5, and 6 are shown when the patient's arm adjacent to the body (supine arm down) or placed above the head (supine arm up) are shown. (A.1, A.2, A.3, A.4, A.5, A.6, A.7, A.8, A.9, A.10)

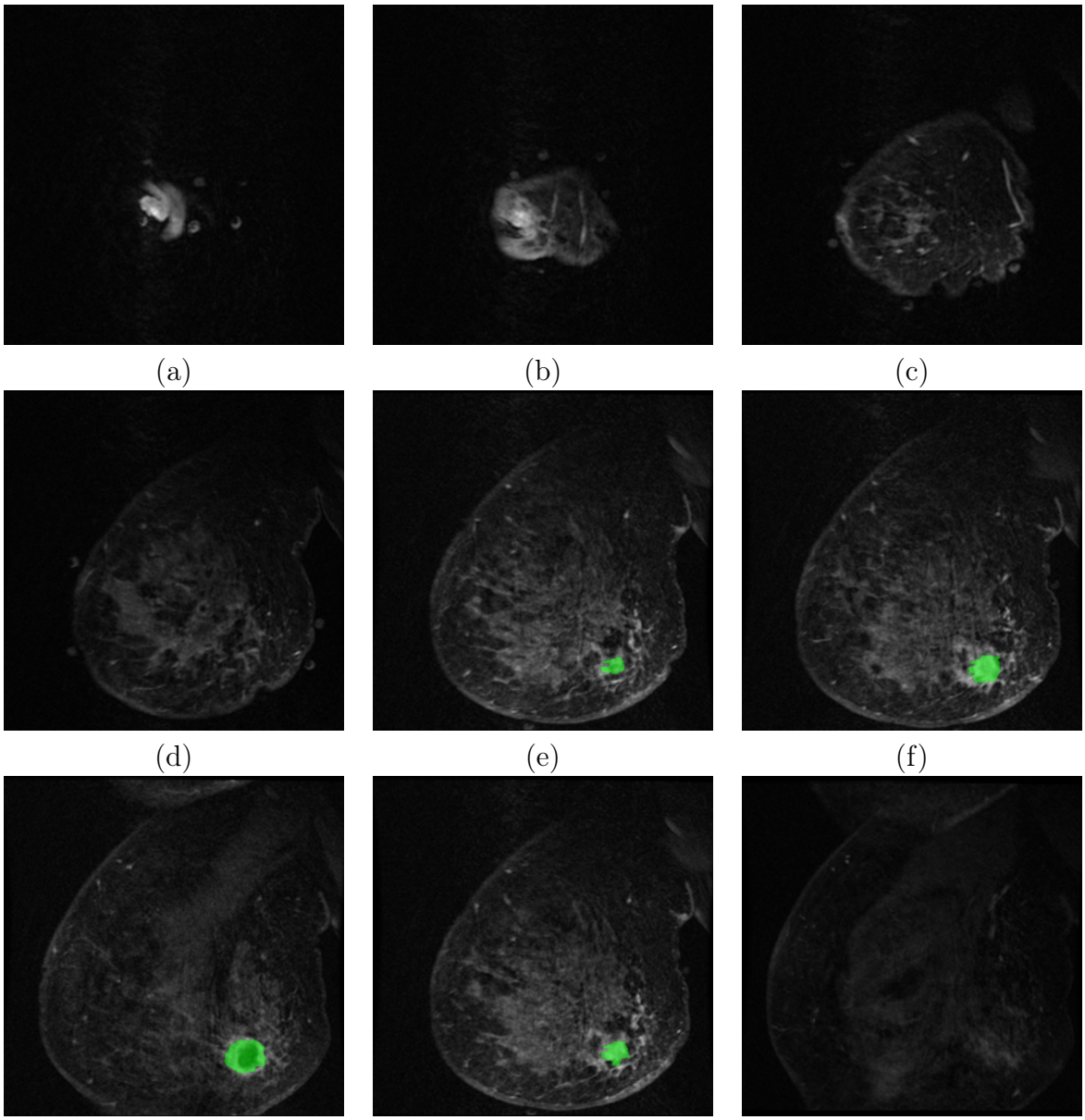

Figure A.1: Patient no. 2; supine arm down, slice no. $6, 10, 15, 25, 29, 34, 38, 46, 50$, respectively.

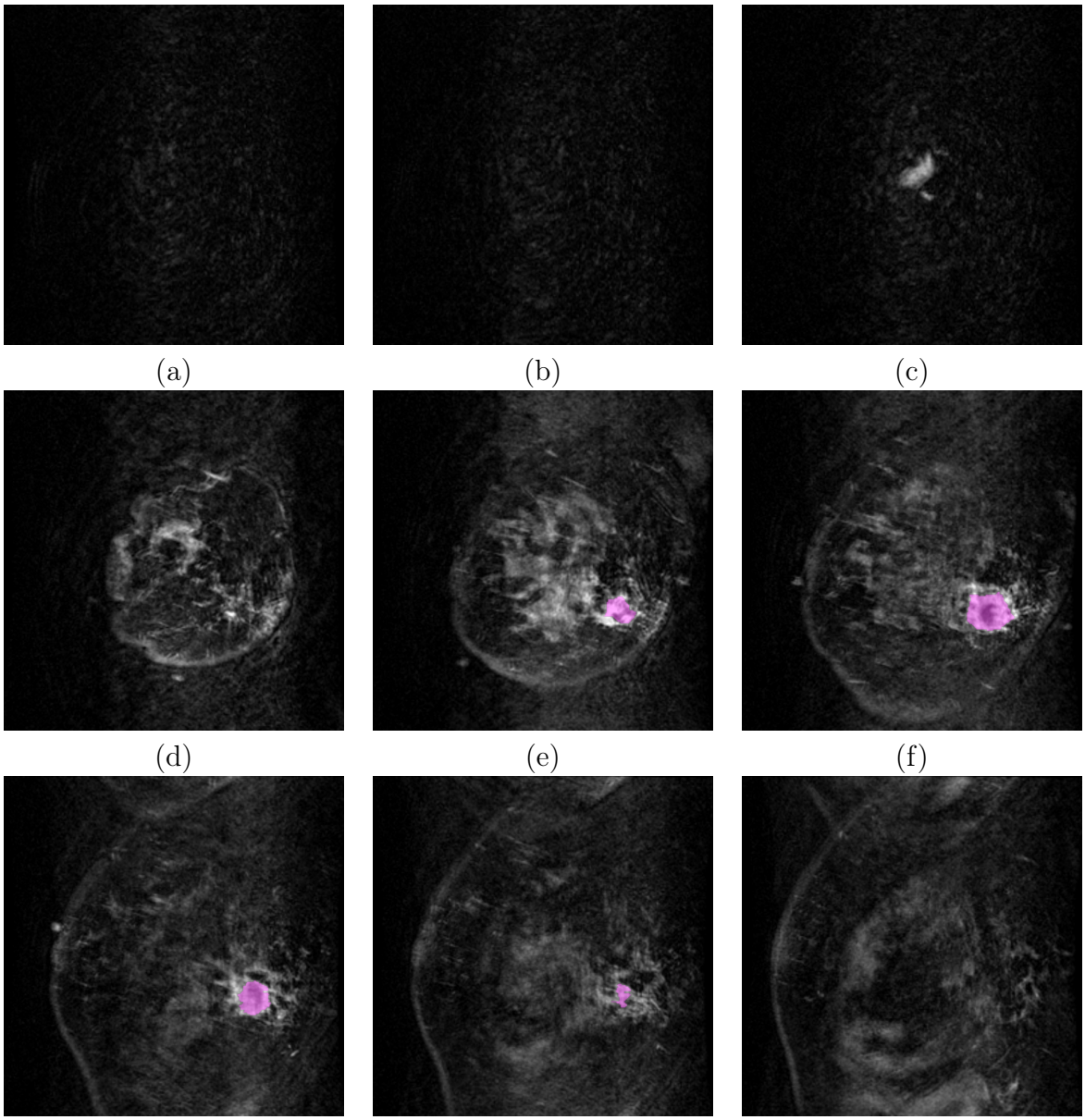

(a) (b) (c)

(d) (e) (f)

(g) (h) (i)

Figure A.2: Patient no. 2; supine arm up, slice no. $6, 10, 15, 25, 29, 34, 38, 46, 50$, respectively.

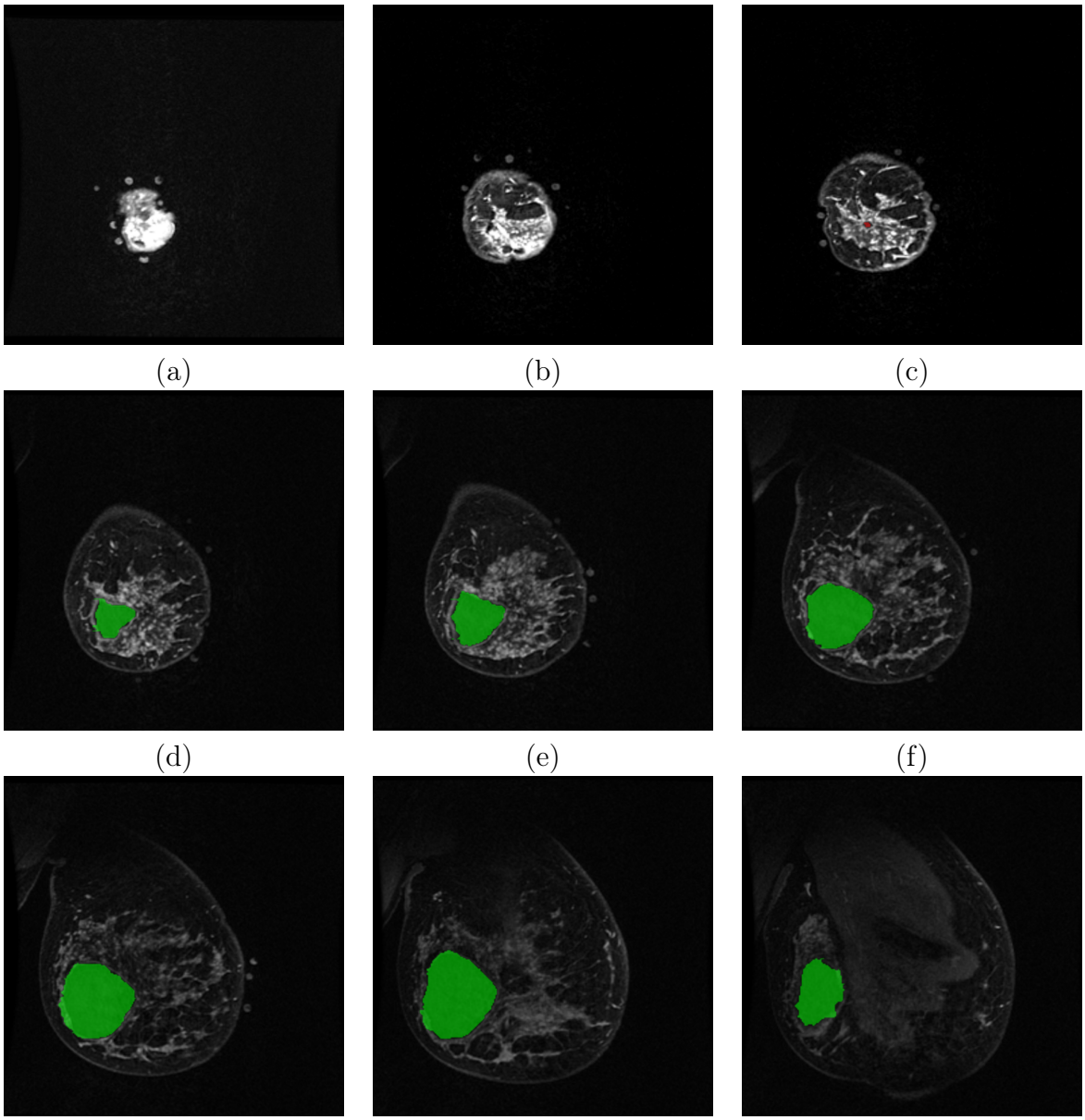

Figure A.3: Patient no. 3; supine arm down, slice no. $5, 10, 15, 19, 23, 30, 35, 45, 55$, respectively.

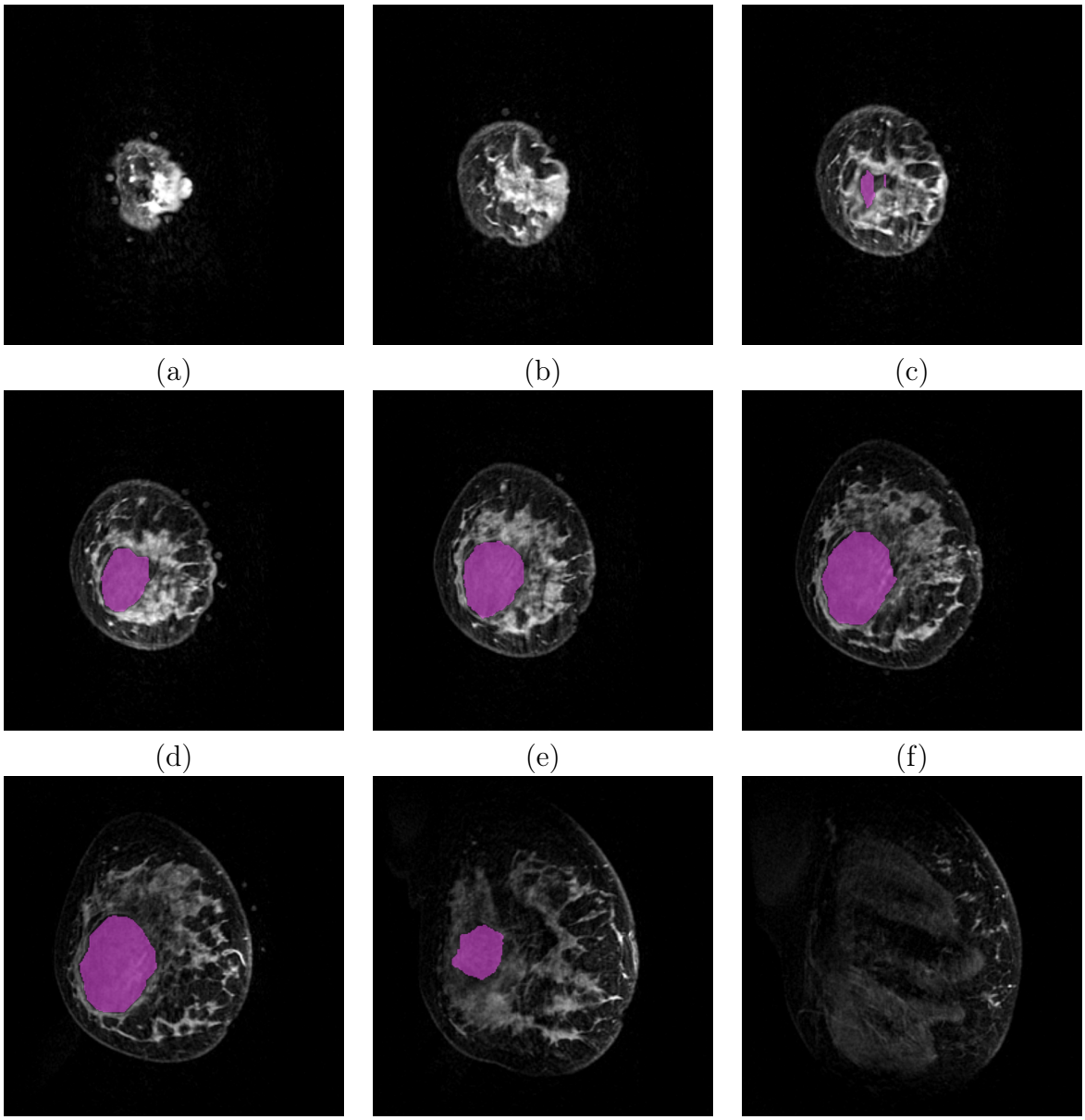

Figure A.4: Patient no. 3; supine arm up, slice no. $5, 10, 15, 19, 23, 30, 35, 45, 55$, respectively.

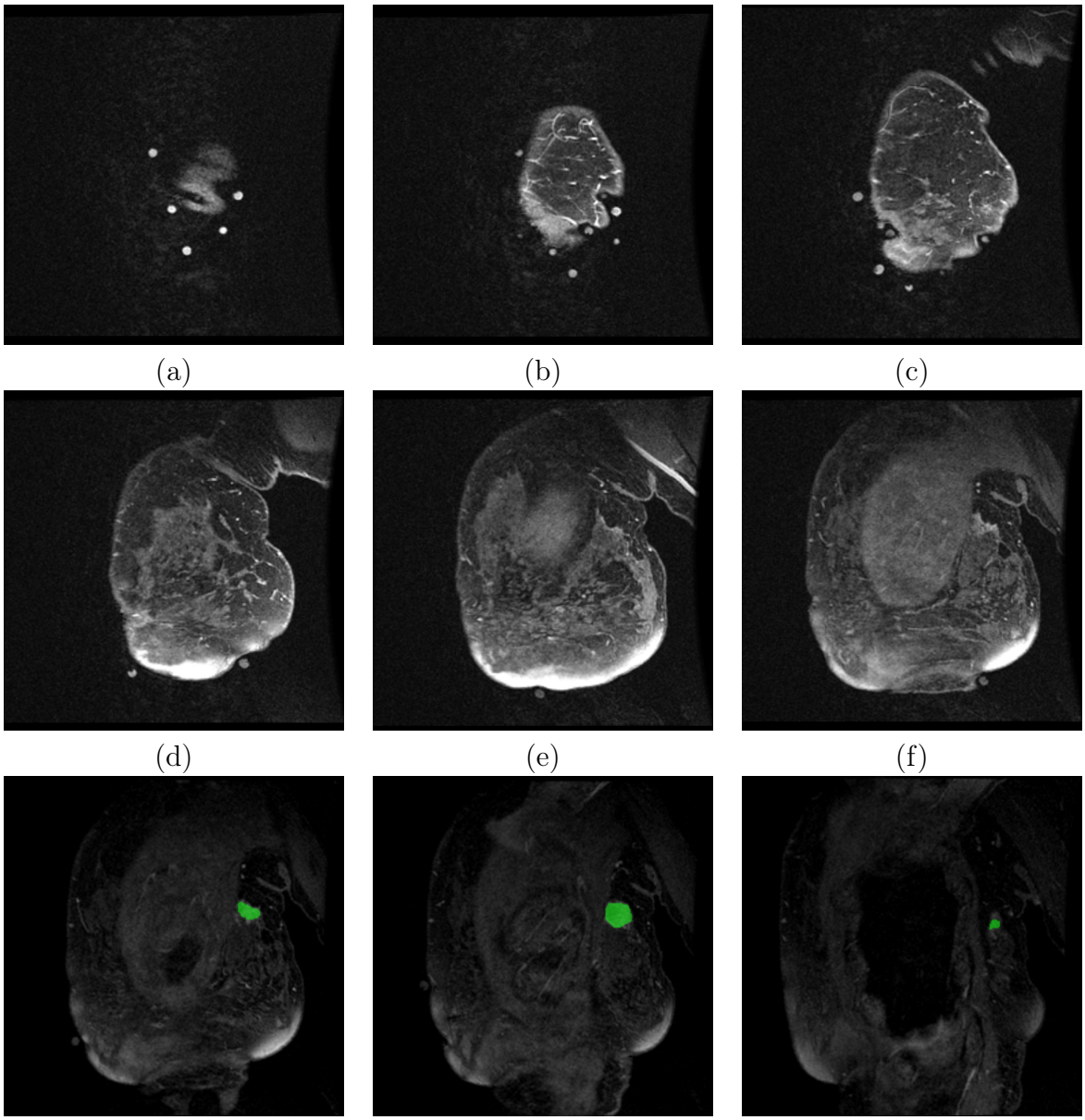

Figure A.5: Patient no. 4; supine arm down, slice no. $5, 10, 15, 20, 27, 32, 34, 38, 45$, respectively.

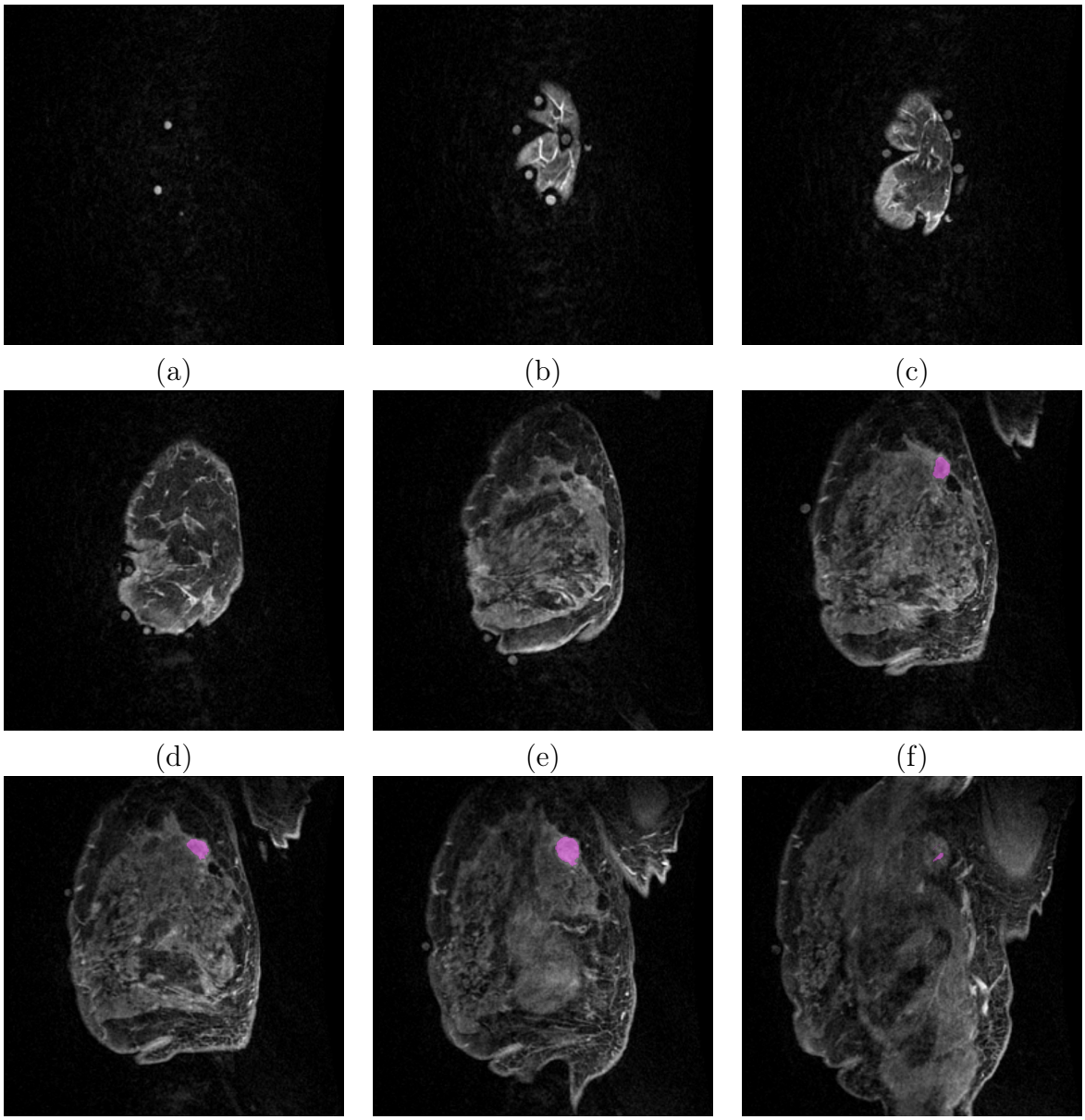

(a) (b) (c)

(d) (e) (f)

(g) (h) (i)

Figure A.6: Patient no. 4; supine arm up, slice no. $5, 10, 15, 20, 27, 32, 34, 38, 45$, respectively.

In this section, the different $3D$ views of tumour in for patient no. 2, 3, 4, 5, 6 are shown. (A.11, A.12, A.13, A.14, A.15)

In this section, the ovelap between the tumours before and after applying the CPD registration methods for patients no. 2, 3, 6; Slice 34 of the $3D$ volume are shown, respectively. (A.17, A.16, A.19, A.18, A.21, A.20)

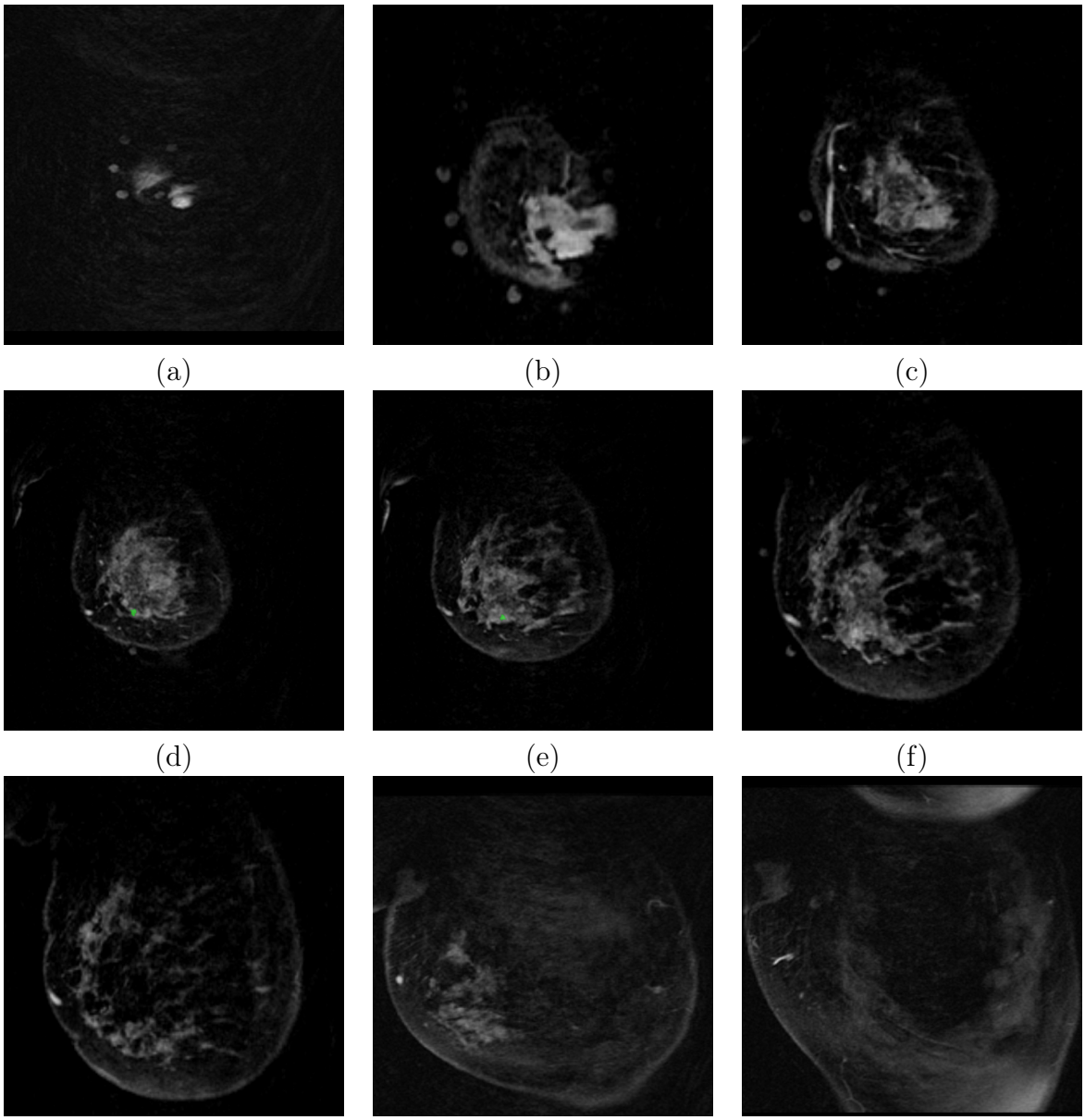

(a) (b) (c)

(d) (e) (f)

(g) (h) (i)

Figure A.7: Patient no. 5; supine arm down, slice no. $6, 10, 15, 18, 23, 25, 30, 40, 50$, respectively.

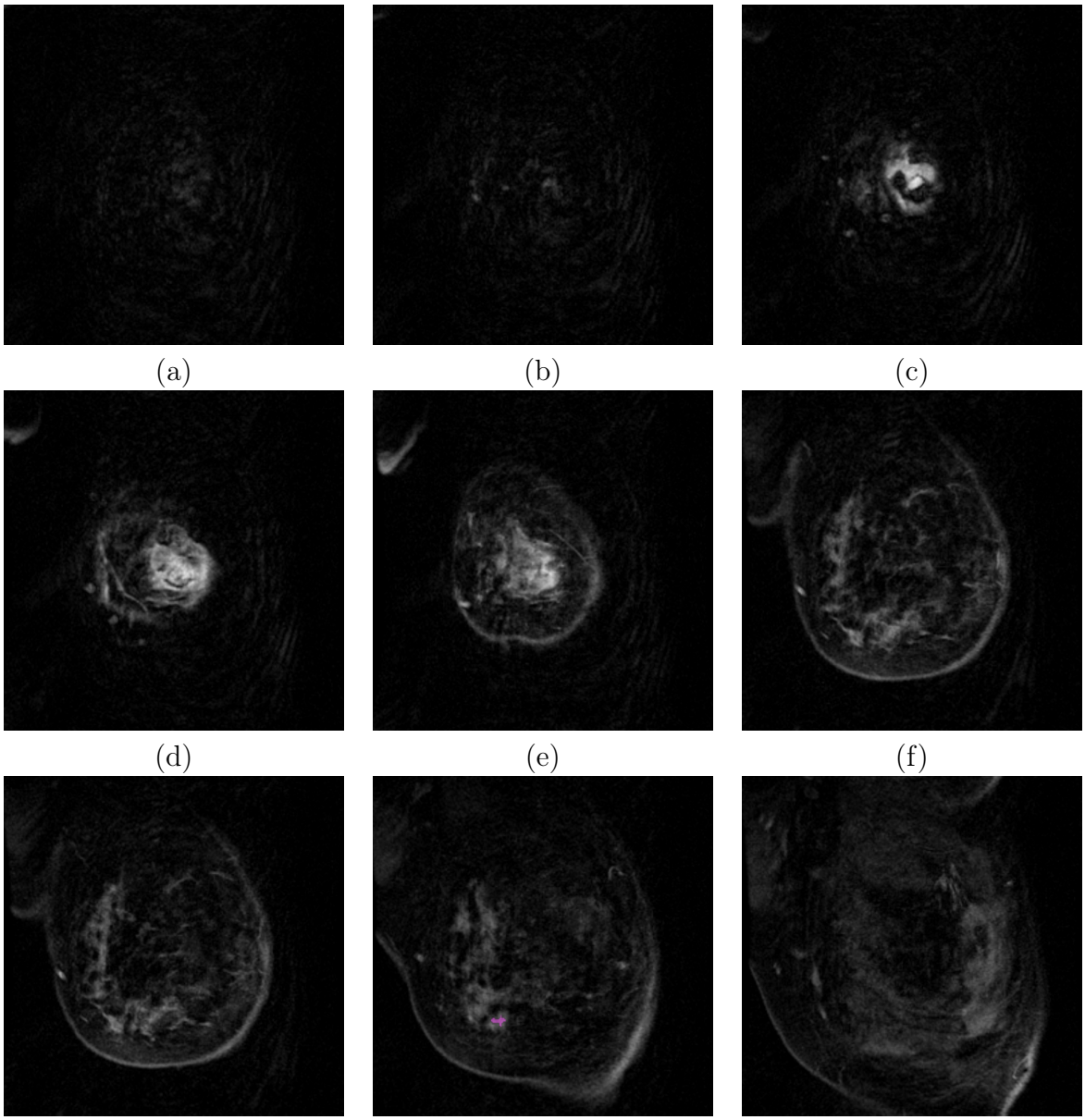

Figure A.8: Patient no. 5; supine arm up, slice no. $6, 10, 15, 18, 23, 25, 30, 40, 50$, respectively.

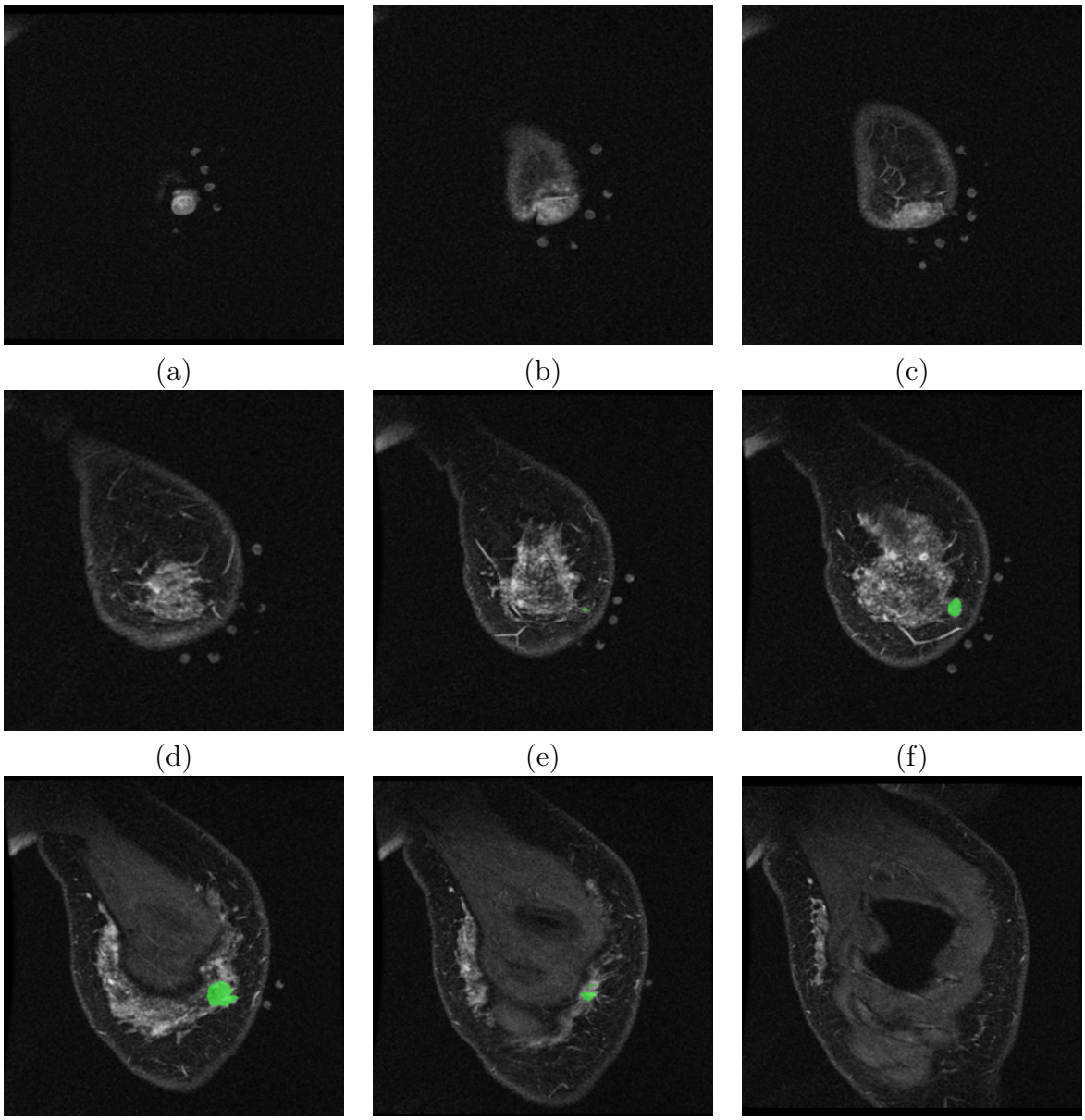

(a) (b) (c)

(d) (e) (f)

(g) (h) (i)

Figure A.9: Patient no. 6; supine arm down, slice no. $5, 10, 15, 21, 23, 26, 34, 40, 45$, respectively.

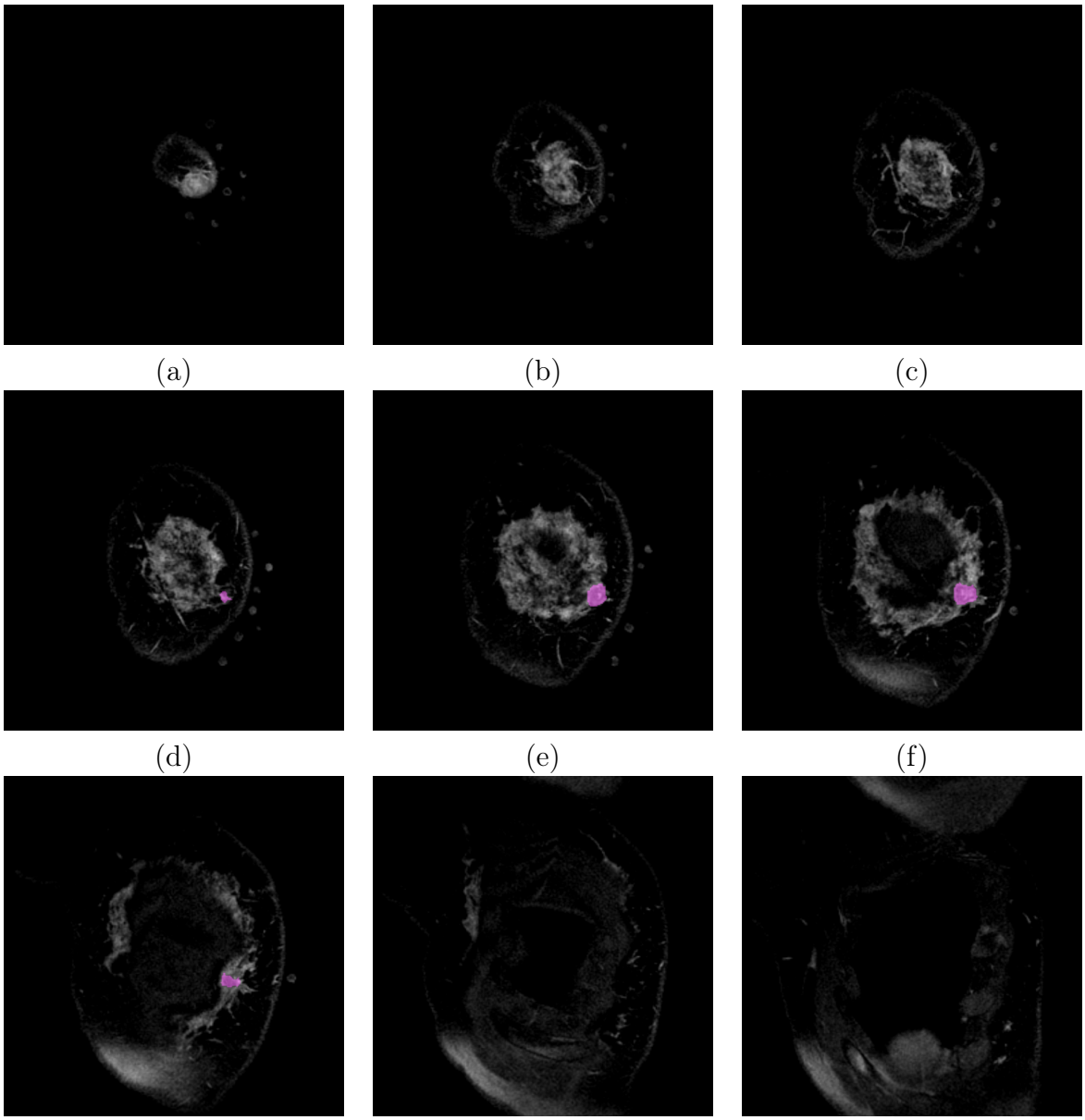

Figure A.10: Patient no. 6; supine arm up, slice no. $5, 10, 15, 21, 23, 26, 34, 40, 45$, respectively.

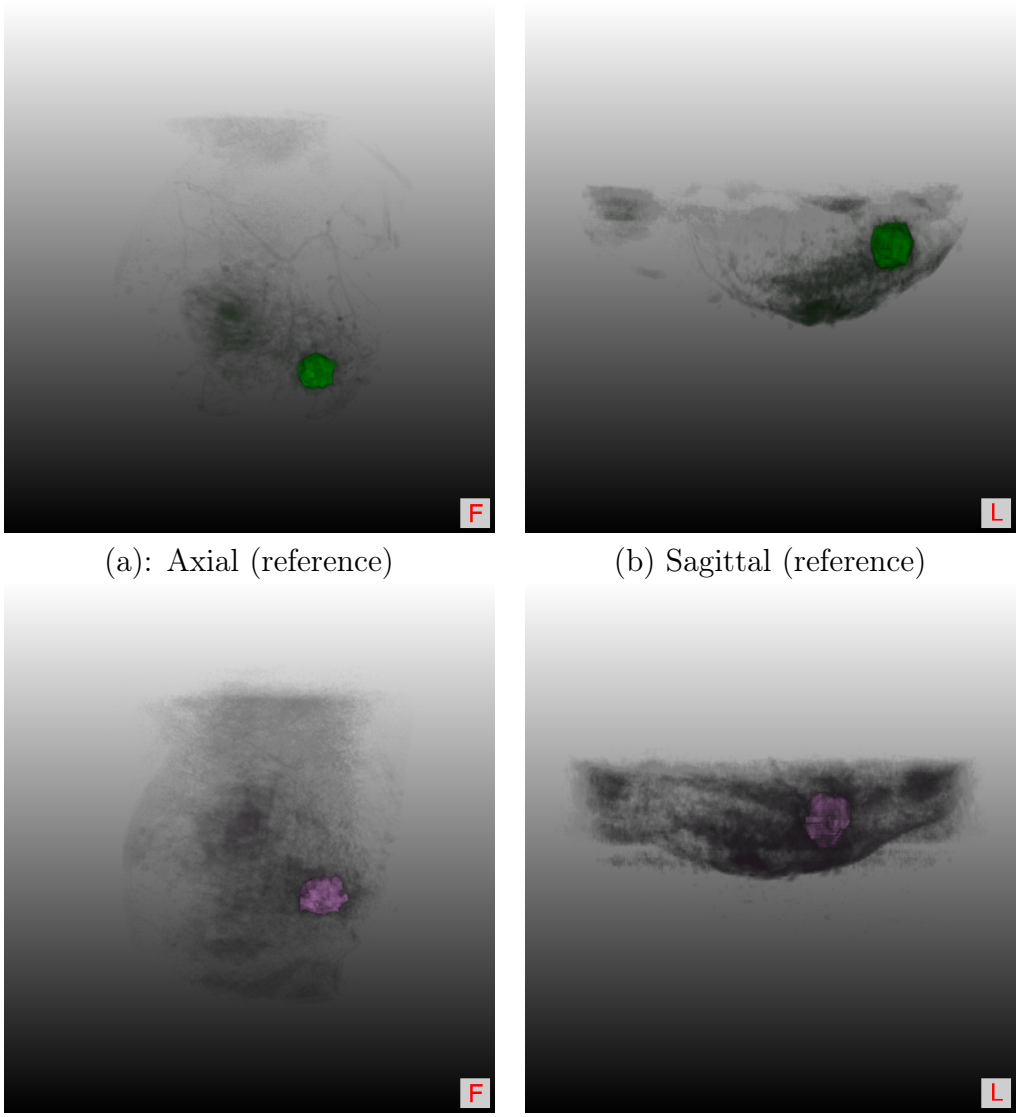

(a): Axial (reference) (b) Sagittal (reference)

(c): Axial (template) (d): Sagittal (template)

Figure A.11: Different $3D$ views of tumour in patient no. 2.

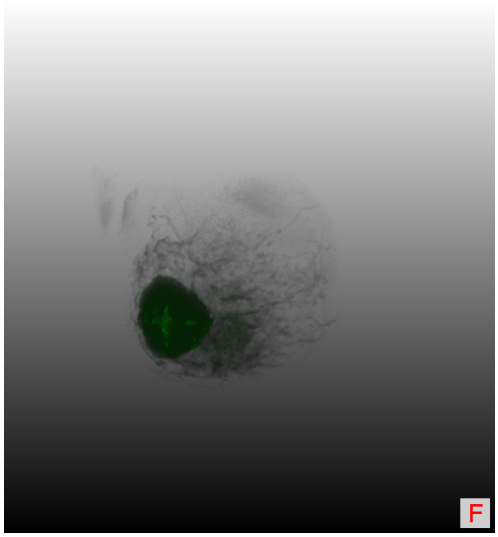

(a): Axial (reference)

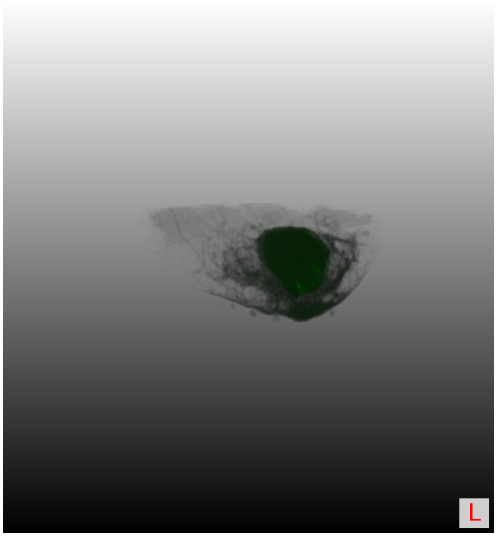

(b): Sagittal (reference)

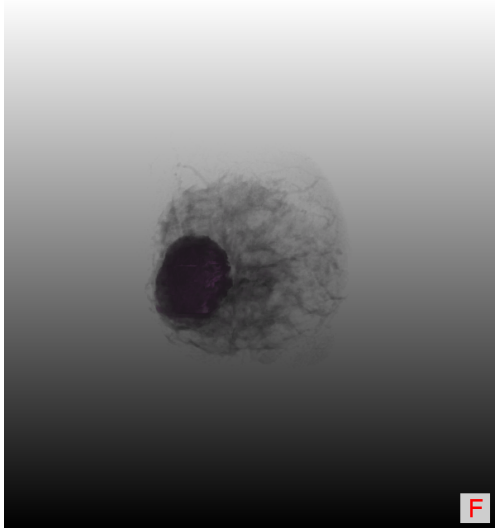

(c): Axial (template)

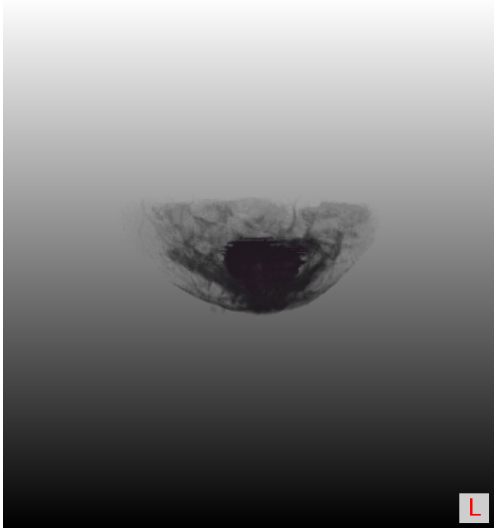

(d): Sagittal (template)

Figure A.12: Different $3D$ views of tumour in patient no. 3.

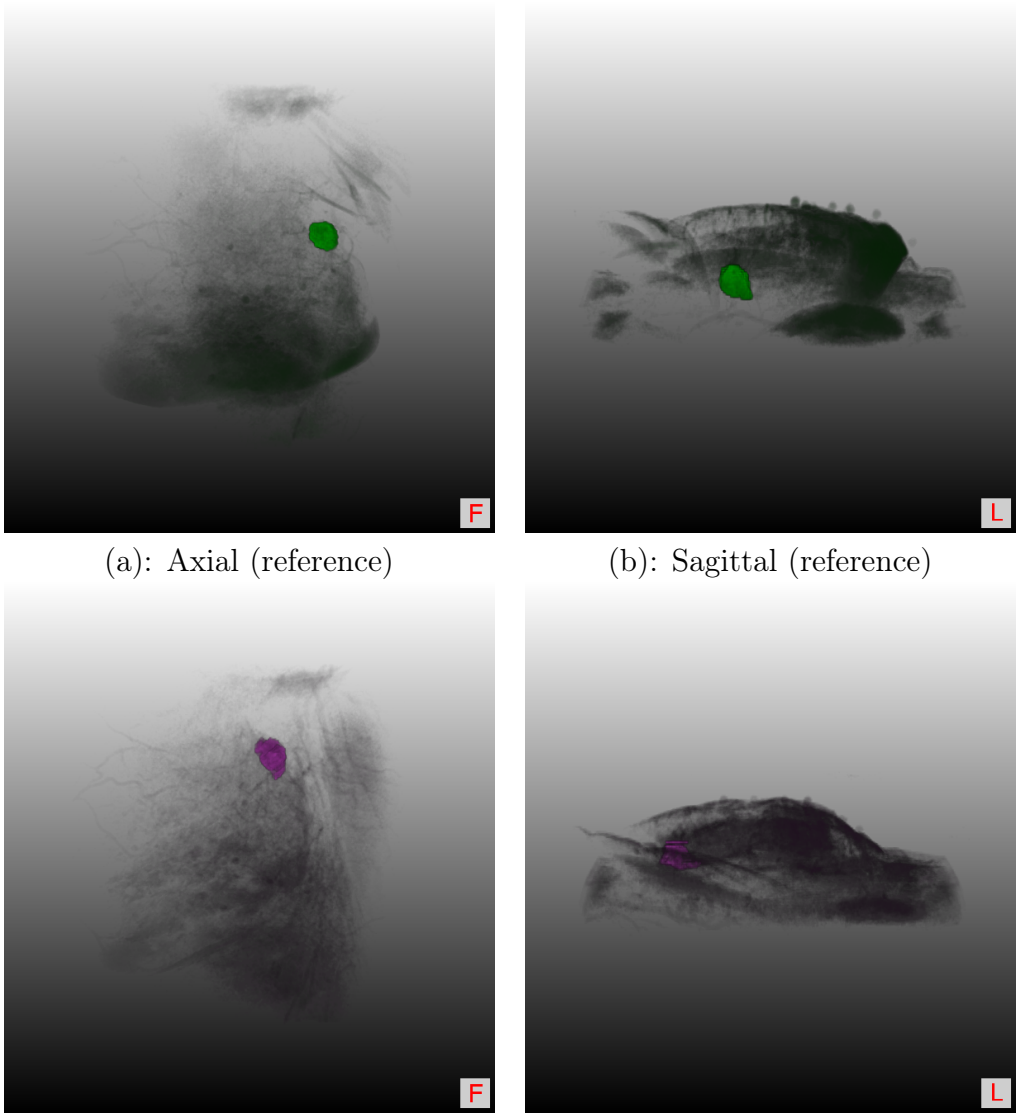

(a): Axial (reference)

(b): Sagittal (reference)

(c): Axial (template)

(d): Sagittal (template)

Figure A.13: Different $3D$ views of tumour in patient no. 4.

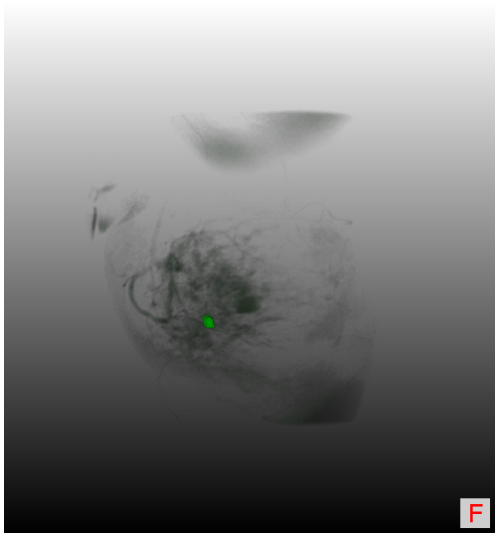

(a): Axial (reference)

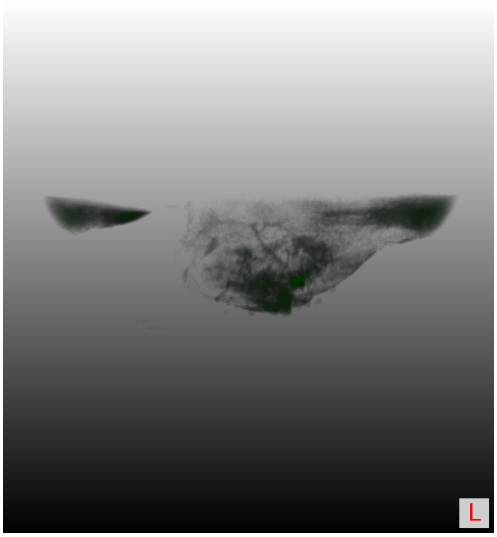

(b): Sagittal (reference)

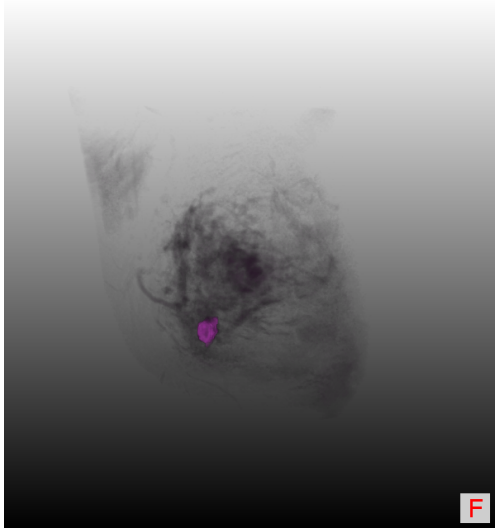

(c): Axial (template)

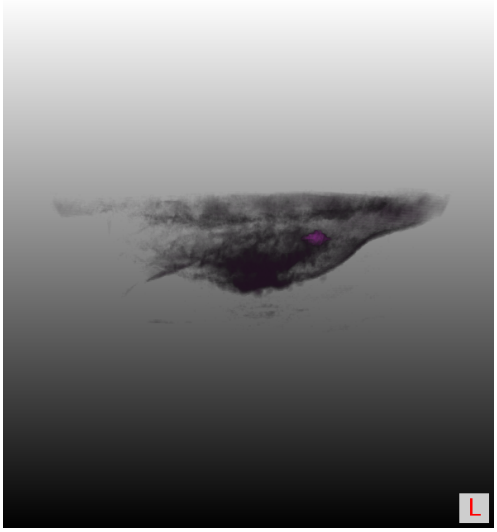

(d): Sagittal (template)

Figure A.14: Different $3D$ views of tumour in patient no. 5.

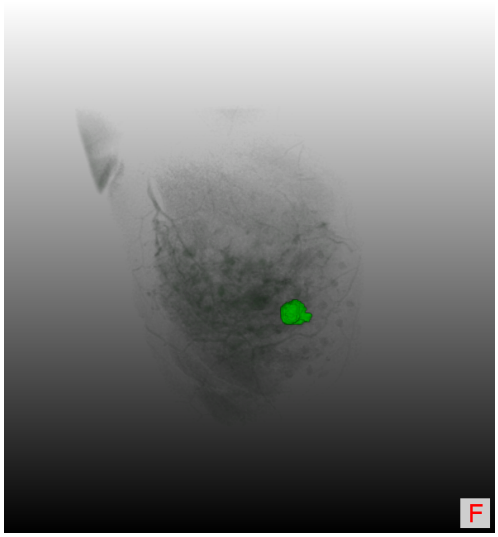

(a): Axial (reference)

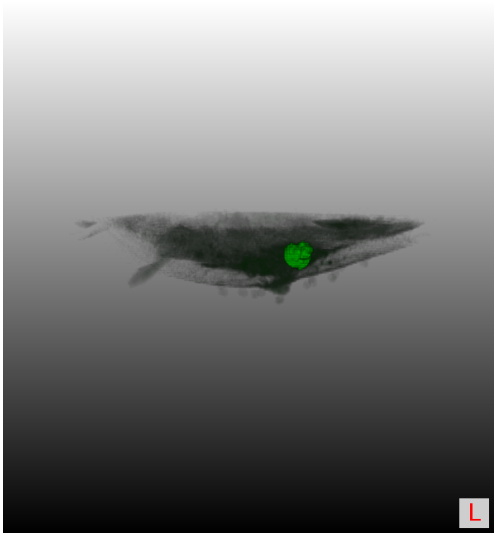

(b): Sagittal (reference)

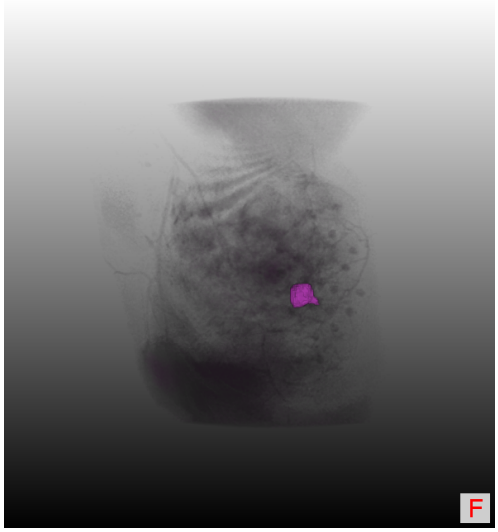

(c): Axial (template)

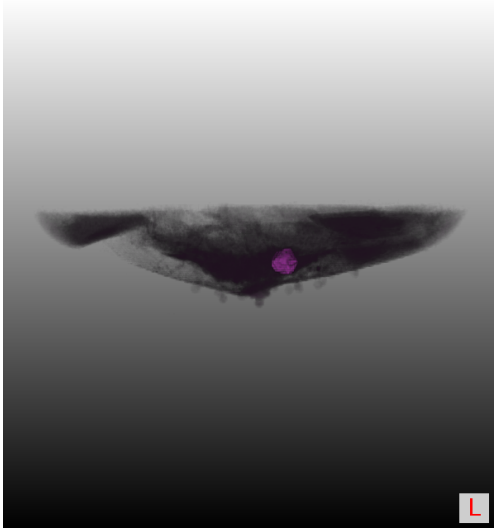

(d): Sagittal (template)

Figure A.15: Different $3D$ views of tumour in patient no. 6.

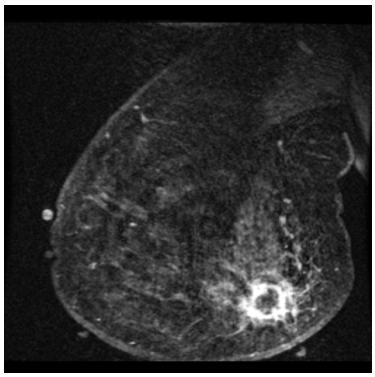

(a) Reference (arm parallel)

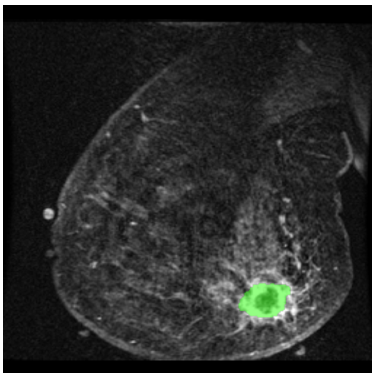

(b) Segmented tumour in reference

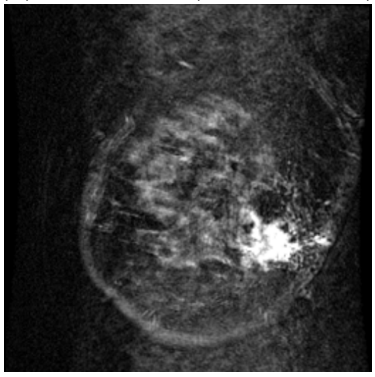

(c) Template (arm up)

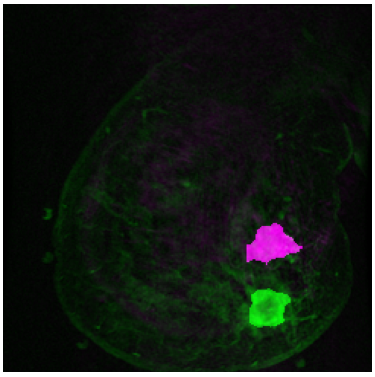

(d) Template overlay on reference

Figure A.16: Patient no. 2 (Before Registration); Slice 34 of the $3D$ volume.

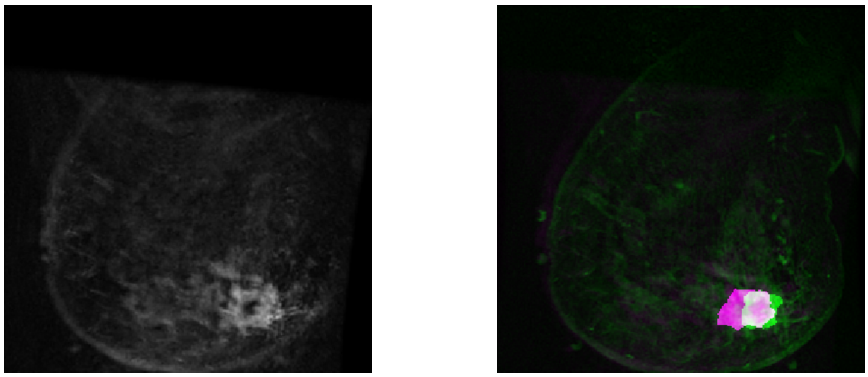

(e) Rigid registered template (f) Rigid registered overlay

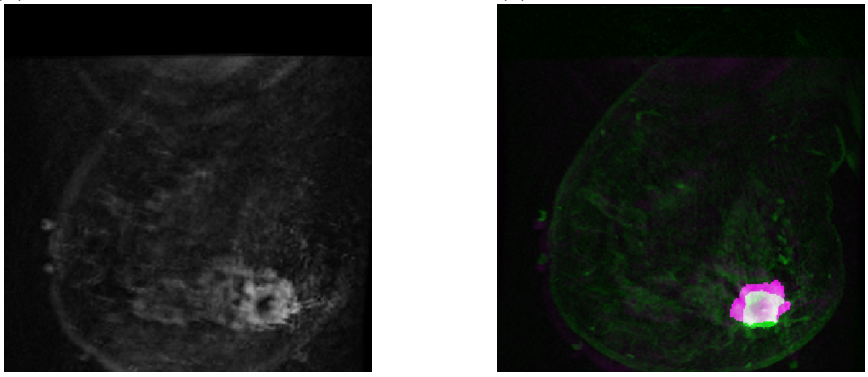

(g) Affine registered template (h) Affine registered overlay

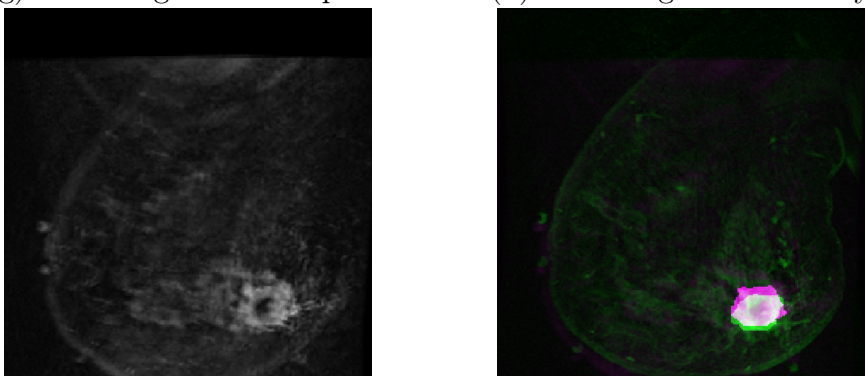

(i) Deformable registered template (j) Deformable registered overlay

Figure A.17: The CPD rigid, affine and deformable registration for patient no. 2; Slice 34 of the $3D$ volume.

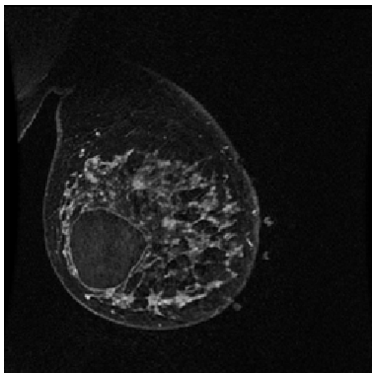

(a) Reference (arm parallel)

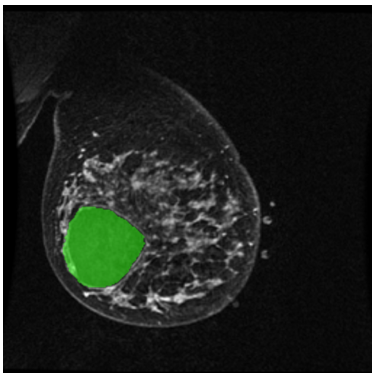

(b) Segmented tumour in reference

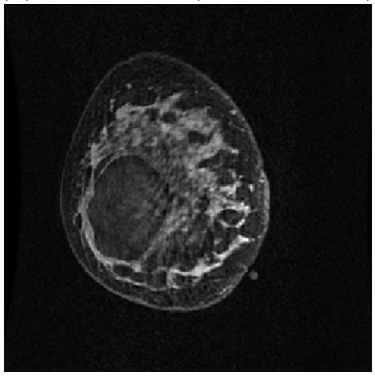

(c) Template (arm up)

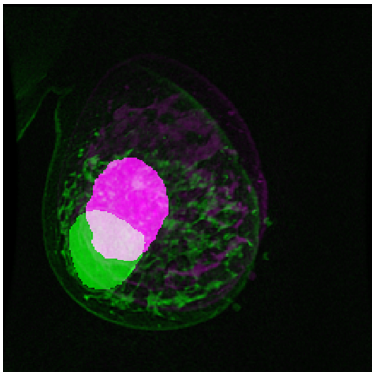

(d) Template overlay on reference

Figure A.18: Patient no. 3 (Before Registration); Slice 34 of the $3D$ volume.

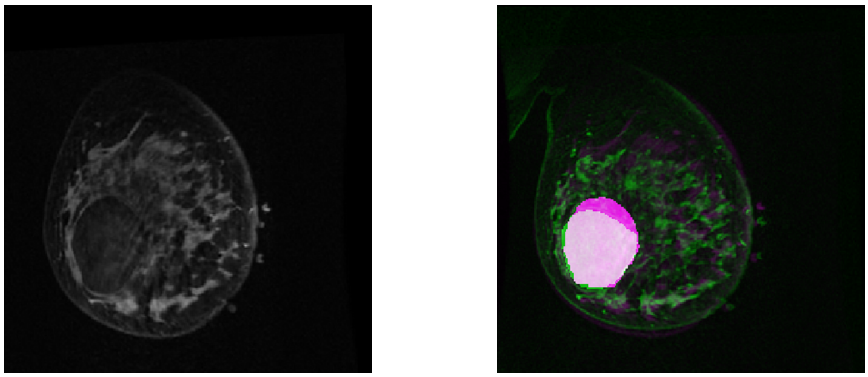

(e) Rigid registered template (f) Rigid registered overlay

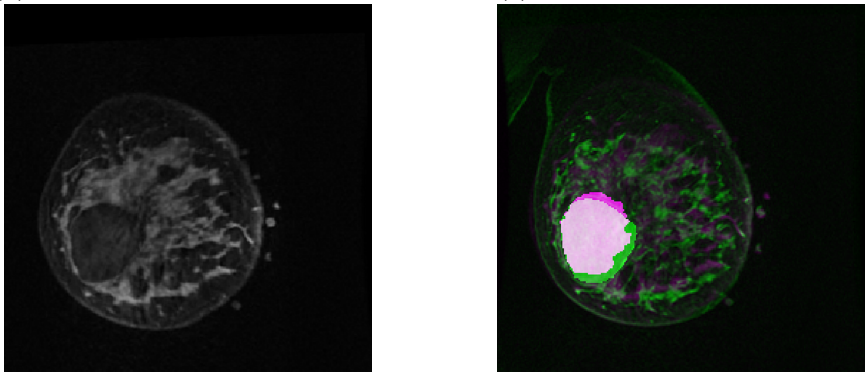

(g) Affine registered template (h) Affine registered overlay

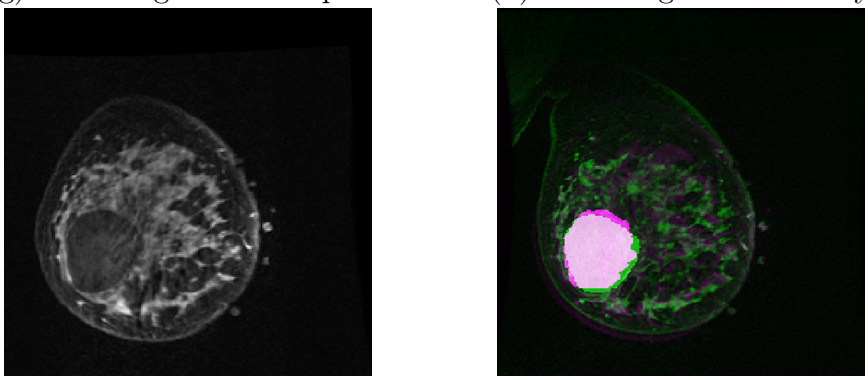

(i) Deformable registered template (j) Deformable registered overlay

Figure A.19: The CPD rigid, affine and deformable registration for patient no. 3; Slice 34 of the $3D$ volume.

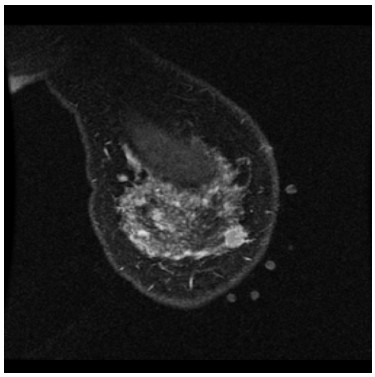

(a) Reference (arm parallel)

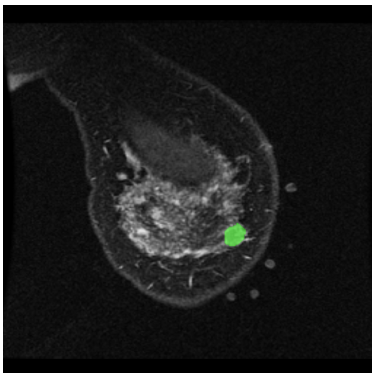

(b) Segmented tumour in reference

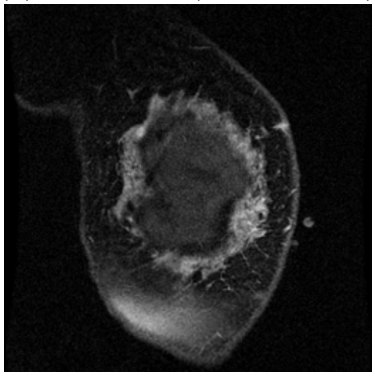

(c) Template (arm up)

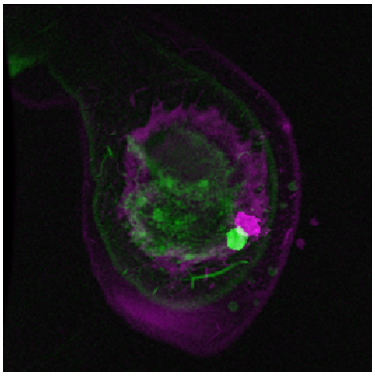

(d) Template overlay on reference

Figure A.20: Patient no. 6 (Before Registration); Slice 26 of the $3D$ volume.

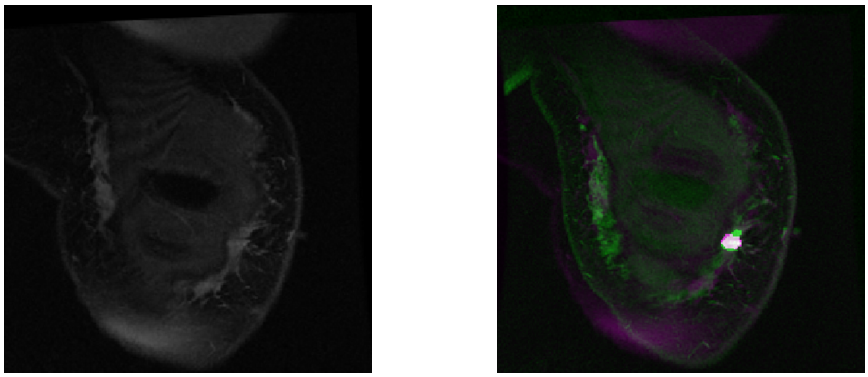

(e) Rigid registered template (f) Rigid registered overlay

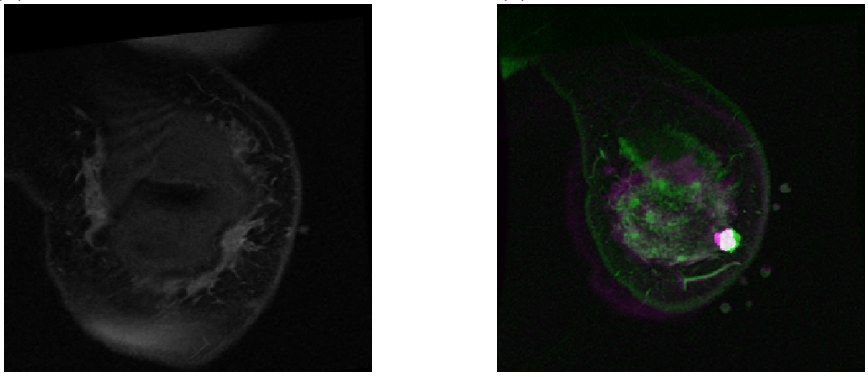

(g) Affine registered template (h) Affine registered overlay

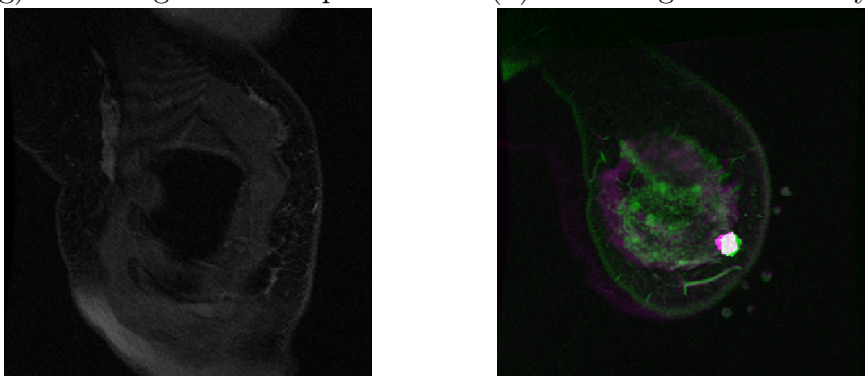

(i) Deformable registered template (j) Deformable registered overlay

Figure A.21: The CPD rigid, affine and deformable registration for patient no. 6; Slice 26 of the $3D$ volume.

References

[B+89] Fred L Bookstein et al. Principal warps: Thin-plate splines and the decomposition of deformations. *IEEE Transactions on pattern analysis and machine intelligence*, 11(6):567–585, 1989.

[BDH96] C Bradford Barber, David P Dobkin, and Hannu Huhdanpaa. The quickhull algorithm for convex hulls. *ACM Transactions on Mathematical Software (TOMS)*, 22(4):469–483, 1996.

[BKZ04] Matt A Bernstein, Kevin F King, and Xiaohong Joe Zhou. *Handbook of MRI pulse sequences*. Elsevier, 2004.

[BM92] Paul J Besl and Neil D McKay. Method for registration of 3-d shapes. In *Robotics-DL tentative*, pages 586–606. International Society for Optics and Photonics, 1992.

[Bro92] Lisa Gottesfeld Brown. A survey of image registration techniques. *ACM computing surveys (CSUR)*, 24(4):325–376, 1992.

[CC78] Edwin Catmull and James Clark. Recursively generated b-spline surfaces on arbitrary topological meshes. *Computer-aided design*, 10(6):350–355, 1978.

[CM92] Yang Chen and Gérard Medioni. Object modelling by registration of multiple range images. *Image and vision computing*, 10(3):145–155, 1992.

[DM56] Abraham De Moivre. *The doctrine of chances: or, A method of calculating the probabilities of events in play*, volume 1. Chelsea Publishing Company, 1756.

[DM77] John E Dennis, Jr and Jorge J Moré. Quasi-newton methods, motivation and theory. *SIAM review*, 19(1):46–89, 1977.

[Duc76] Jean Duchon. Interpolation des fonctions de deux variables suivant le principe de la flexion des plaques minces. *Revue française d'automatique, informatique, recherche opérationnelle. Analyse numérique*, 10(3):5–12, 1976.

[ESM+14] Mehran Ebrahimi, Peter Siegler, Amen Modhafar, Claire MB Holloway, Donald B Plewes, and Anne L Martel. Using surface markers for mri guided breast conserving surgery: a feasibility survey. *Physics in medicine and biology*, 59(7):1589, 2014.

[HM04] Eldad Haber and Jan Modersitzki. Numerical methods for volume preserving image registration. *Inverse problems*, 20(5):1621, 2004.

[JCDW10] Ahmedin Jemal, Melissa M Center, Carol DeSantis, and Elizabeth M Ward. Global patterns of cancer incidence and mortality rates and trends. *Cancer Epidemiology Biomarkers & Prevention*, 19(8):1893–1907, 2010.

[LH03] Bin Luo and Edwin R Hancock. A unified framework for alignment and correspondence. *Computer Vision and Image Understanding*, 92(1):26–55, 2003.

[LLC09a] MultiMedia LLC. MS Windows NT breast anatomy. `http://healthforself.today.com/2009/03/22/breast-cancer`, 2009. Accessed: 2009-03-22.

[LLC09b] MultiMedia LLC. MS Windows NT breast mri. `https://doi.org/10.2147/RMI.S46800`, 2009. Accessed: 2014-09-09.

[ML05] Elizabeth Morris and Laura Liberman. *Breast MRI: diagnosis and intervention*, volume 255. Springer Science & Business Media, 2005.

[Mod09] Jan Modersitzki. *FAIR: flexible algorithms for image registration*, volume 6. SIAM, 2009.

[Møl93] Martin Fodslette Møller. A scaled conjugate gradient algorithm for fast supervised learning. *Neural networks*, 6(4):525–533, 1993.

[MS10] Andriy Myronenko and Xubo Song. Point set registration: Coherent point drift. *IEEE transactions on pattern analysis and machine intelligence*, 32(12):2262–2275, 2010.

[MSCP06] Andriy Myronenko, Xubo Song, and Miguel A Carreira-Perpinán. Non-rigid point set registration: Coherent point drift. In *Advances in Neural Information Processing Systems*, pages 1009–1016, 2006.

[MV98] JB Antoine Maintz and Max A Viergever. A survey of medical image registration. *Medical image analysis*, 2(1):1–36, 1998.

[MvdEV96] J. B. Antoine Maintz, Petra A van den Elsen, and Max A. Viergever. Evaluation of ridge seeking operators for multimodality medical image

matching. *IEEE Transactions on pattern analysis and machine intelligence*, 18(4):353–365, 1996.

[NW06] Jorge Nocedal and Stephen Wright. *Numerical optimization*. Springer Science & Business Media, 2006.

[PBSS00] Donald B Plewes, Jonathan Bishop, Abbas Samani, and Justin Sciarretta. Visualization and quantification of breast cancer biomechanical properties with magnetic resonance elastography. *Physics in medicine and biology*, 45(6):1591, 2000.

[Pea94] Karl Pearson. Contributions to the mathematical theory of evolution. *Philosophical Transactions of the Royal Society of London. A*, 185:71–110, 1894.

[PH77] Franco P. Preparata and Se June Hong. Convex hulls of finite sets of points in two and three dimensions. *Communications of the ACM*, 20(2):87–93, 1977.

[SF00] Milan Sonka and J Michael Fitzpatrick. Volume 2, medical image processing and analysis. In *Handbook of medical imaging*. SPIE - The international society for optical engineering, 2000.

[SLZ+12] Lin Shi, Wen Liu, Heye Zhang, Yongming Xie, and Defeng Wang. A survey of gpu-based medical image computing techniques. *Quantitative imaging in medicine and surgery*, 2(3):188–206, 2012.

[SoCACoRR87] Canadian Cancer Society, National Cancer Institute of Canada. Advisory Committee on Records, and Registries. *Canadian cancer statistics*. Canadian Cancer Society, 1987.

[Sti86] Stephen M Stigler. *The history of statistics: The measurement of uncertainty before 1900*. Harvard University Press, 1986.

[Tan05] Christine Tanner. *Registration and lesion classification of contrast-enhanced magnetic resonance breast images*. PhD thesis, School of Medicine, King's College London, 2005.

[THA11] Andrew Top, Ghassan Hamarneh, and Rafeef Abugharbieh. Active learning for interactive 3d image segmentation. In *International Conference on Medical Image Computing and Computer-Assisted Intervention*, pages 603–610. Springer, 2011.

[TSM85] D Michael Titterington, Adrian FM Smith, and Udi E Makov. *Statistical analysis of finite mixture distributions*. Wiley,, 1985.

[UN98] Naonori Ueda and Ryohei Nakano. Deterministic annealing em algorithm. *Neural networks*, 11(2):271–282, 1998.

[ZF03] Barbara Zitova and Jan Flusser. Image registration methods: a survey. *Image and vision computing*, 21(11):977–1000, 2003.